

Moving mesh cosmology: characteristics of galaxies and haloes

Dušan Kereš^{1,2*}, Mark Vogelsberger³, Debora Sijacki^{3†}, Volker Springel^{4,5}, Lars Hernquist³

¹*Department of Astronomy and Theoretical Astrophysics Center, University of California, Berkeley, CA 94720-3411, USA*

²*Department of Physics, Center for Astrophysics and Space Sciences, University of California at San Diego, 9500 Gilman Drive, La Jolla, CA 92093, USA*

³*Harvard-Smithsonian Center for Astrophysics, 60 Garden Street, Cambridge, MA 02138, USA*

⁴*Heidelberg Institute for Theoretical Studies, Schloss-Wolfsbrunnengasse 35, 69118 Heidelberg, Germany*

⁵*Zentrum für Astronomie der Universität Heidelberg, ARI, Mönchhofstr. 12-14, 69120 Heidelberg, Germany*

24 July 2012

ABSTRACT

We discuss cosmological hydrodynamic simulations of galaxy formation performed with the new moving-mesh code AREPO, which promises higher accuracy compared with the traditional SPH technique that has been widely employed for this problem. In this exploratory study, we deliberately limit the complexity of the physical processes followed by the code for ease of comparison with previous calculations, and include only cooling of gas with a primordial composition, heating by a spatially uniform UV background, and a simple sub-resolution model for regulating star formation in the dense interstellar medium. We use an identical set of physics in corresponding simulations carried out with the well-tested SPH code GADGET, adopting also the same high-resolution gravity solver. We are thus able to compare both simulation sets on an object-by-object basis, allowing us to cleanly isolate the impact of different hydrodynamical methods on galaxy and halo properties. In accompanying papers, we focus on an analysis of the global baryonic statistics predicted by the simulation codes (Vogelsberger et al. 2011), and complementary idealized simulations that highlight the differences between the hydrodynamical schemes (Sijacki et al. 2011). Here we investigate their influence on the baryonic properties of simulated galaxies and their surrounding haloes. We find that AREPO leads to significantly higher star formation rates for galaxies in massive haloes and to more extended gaseous disks in galaxies, which also feature a thinner and smoother morphology than their GADGET counterparts. Consequently, galaxies formed in AREPO have larger sizes and higher specific angular momentum than their SPH correspondents. Interestingly, the more efficient cooling flows in AREPO yield higher densities and lower entropies in halo centers compared to GADGET, whereas the opposite trend is found in halo outskirts. The cooling differences leading to higher star formation rates of massive galaxies in AREPO also slightly increase the baryon content within the virial radius of massive haloes. We show that these differences persist as a function of numerical resolution. While both codes agree to acceptable accuracy on a number of baryonic properties of cosmic structures, our results thus clearly demonstrate that galaxy formation simulations greatly benefit from the use of more accurate hydrodynamical techniques such as AREPO and call into question the reliability of galaxy formation studies in a cosmological context using traditional standard formulations of SPH, such as the one implemented in GADGET. Our new moving-mesh simulations demonstrate that a population of extended gaseous disks of galaxies in large volume cosmological simulations can be formed even without energetic feedback in the form of galactic winds, although such outflows appear required to obtain realistic stellar masses.

Key words: cosmology: dark matter – methods: numerical – galaxies: evolution – galaxies: formation – galaxies: haloes

1 INTRODUCTION

Cosmological simulations of galaxy formation provide a powerful technique to calculate the non-linear evolution of structure forma-

* Hubble Fellow. E-mail: dkeres@physics.ucsd.edu

† Hubble Fellow.

tion. In principle, such simulations can properly model the evolution and formation of galaxies from first principles, but the enormous dynamic range and the many poorly understood aspects of the baryonic physics of star formation make this task extremely challenging. At present, the limitations imposed by the coarse numerical resolution achievable in practice and by the approximate treatment of the physics introduce significant uncertainties in simulation predictions. Regardless, previous simulations have already proven instrumental for developing our current understanding of the formation and evolution of galaxies (e.g. Katz et al. 1992; Weinberg et al. 1997; Pearce et al. 1999; Kravtsov et al. 2002; Springel & Hernquist 2003a,b; Borgani et al. 2004; Crain et al. 2009).

When only dark matter (DM) is considered, the newest generation of cosmological simulation codes yields a consensus picture of important key results about the matter distribution in the Universe, such as the large-scale distribution and the detailed internal properties of dark matter haloes (Springel et al. 2005, 2008; Diemand et al. 2008; Boylan-Kolchin et al. 2009; Navarro et al. 2010; Klypin et al. 2010). The computational methods employed in the codes vary between different implementations; however, the discretization of the equations needed to follow the evolution of DM involves only gravity, and can only be done efficiently in terms of the N-body technique. Hence the requirements for obtaining converged and consistent results with different simulation codes are clear; all that is needed is an accurate gravity solver, a sufficiently large number of simulation particles and an accurate time integration scheme.

Over the last decades, a number of hydrodynamic codes have been developed and used in the field of computational cosmology (e.g. Ryu et al. 1993; Bryan et al. 1995; Katz et al. 1996; Springel et al. 2001; Teyssier 2002; Wadsley et al. 2004; Springel 2005). They all account for the baryons in the Universe and try to follow their evolution self-consistently in a Λ CDM dominated universe by solving the equations of hydrodynamics coupled to gravity. However, the discretization schemes and numerical algorithms used for this task differ widely from code to code, and unlike in pure DM simulations, large differences in the simulation outcomes are often found. Such simulations can be more directly related to observations, unlike the pure dark matter simulations.

In fact, hydrodynamic simulations have already explained several features of the observed large scale distribution of baryons, such as the existence and the properties of the Ly- α forest in the spectra of distant QSOs (e.g. Hernquist et al. 1996; Miralda-Escudé et al. 1996). In this, low density, low temperature regime different hydrodynamic techniques show good agreement between SPH and grid-based codes (Regan et al. 2007). Numerical simulations played a crucial role in both our understanding of the properties of the absorbing gas and in the quantitative measurements of the matter distribution in the Universe based on Lyman- α forest data (e.g. Croft et al. 1998; Seljak et al. 2005).

Unfortunately, at higher densities characteristic of galaxies and their haloes, qualitative differences exist already at the simplest modeling level where radiative gas cooling and energetic feedback processes due to star formation are ignored (e.g. Frenk et al. 1999; O’Shea et al. 2005; Agertz et al. 2007; Tasker et al. 2008; Vazza et al. 2011). Such differences are sometimes apparent even between codes using quite similar discretization techniques (Springel & Hernquist 2002; Keres 2007). This emphasizes the need to find numerical methods that give the most accurate and reliable results. Understanding the origin and size of errors in a given computational technique is clearly vital for fully exploiting the predictive power of cosmological simulations of galaxy formation.

The most widely used methods to follow the evolution of baryons in cosmological simulations are Lagrangian smoothed particle hydrodynamics (SPH) and Eulerian mesh-based hydrodynamics with adaptive mesh refinement (AMR). SPH has the great advantage of being naturally adaptive, making it suitable for simulations with a large dynamic range in density, such as cosmological simulations where SPH automatically increases its resolution in collapsing regions. In addition, SPH can be easily combined with very accurate gravity solvers, which are often based on gravitational tree algorithms (e.g. Hernquist & Katz 1989) or particle-mesh+tree (e.g. Bagla 2002; Springel 2005) methods. SPH has excellent conservation properties. In particular, it still manifestly conserves total energy even when coupled to self-gravity, something not available in hydrodynamical mesh codes (Müller & Steinmetz 1995). On the other hand, AMR codes offer higher accuracy in representing shocks, large density gradients and hydrodynamic fluid instabilities (e.g. Agertz et al. 2007).

It has become clear over recent years that both SPH and AMR codes suffer from weaknesses which are likely the primary cause for the disagreements found in some cosmological results obtained with these methods (e.g. Mitchell et al. 2009). For example, it has been shown that SPH in its standard implementation has limited ability to accurately follow fluid instabilities (Ageretz et al. 2007). Furthermore, in SPH, shock capturing is done through the addition of an artificial viscosity, which increases the dissipativeness of the scheme and can have unwanted consequences such as angular momentum transport in disks. Also, while the introduction of an artificial viscosity results in the correct properties of post-shock flow, the width of a shock in SPH can be significantly broadened (e.g. Hernquist & Katz 1989), potentially affecting the evolution of gas in complex cosmological environments (Hutchings & Thomas 2000), for example causing in-shock cooling (Creasey et al. 2011). On the other hand, Eulerian AMR codes are not free of unwanted numerical effects either. They may suffer from advection errors, mesh-alignment effects, and potentially over-mixing (Wadsley et al. 2008). In addition, AMR codes are intrinsically not Galilean-invariant, i.e. their truncation error depends on the bulk velocity relative to the grid. This can be a significant issue when the velocities of the flow are large and the resolution is limited (e.g. Springel 2010a; Robertson et al. 2010).

Recently, Springel (2010a) (S10 hereafter) proposed a new “moving-mesh” technique that promises accuracy advantages over both of these traditional approaches. This new method has been realized in the AREPO code and can be viewed as a hybrid of Lagrangian SPH and Eulerian AMR, combining positive features of both methods while avoiding their most important weaknesses. Instead of a stationary structured mesh as in AMR codes, AREPO uses an unstructured mesh given by the Voronoi tessellation of a set of mesh-generating points distributed within the computational domain. These points are allowed to move with the fluid, causing the mesh to be moved along as well, so that a natural adaptivity is achieved, just as in SPH. On the other hand, AREPO employs the same concepts of spatial reconstruction and Riemann-solver based flux computation as ordinary AMR codes, thereby retaining their high accuracy for shocks and fluid instabilities, and their low level of numerical dissipation. In addition, because the mesh can move with the fluid, the numerical solutions of AREPO are fully Galilean-invariant and have lower advection errors compared to codes with a stationary mesh.

The AREPO code has already been successfully used in problems of first star formation (Greif et al. 2011), and extensions for radiative transfer (Petkova & Springel 2011) and magnetohy-

hydrodynamics (Pakmor et al. 2011) exist. Here we apply this new method for the first time to cosmological galaxy formation simulations in representative parts of the Universe. In what follows, we are primarily interested in clarifying to which extent the new hydrodynamic solver affects the properties of galaxies when compared to the widely employed SPH code GADGET (last described in Springel 2005). GADGET shares an identical high-resolution Tree-PM gravity solver with AREPO, allowing us to study differences caused by the hydrodynamics alone, unaffected by possible systematics in the gravitational dynamics of the collisionless components, which were present in previous comparisons of mesh-based and SPH techniques (e.g. O’Shea et al. 2005; Heitmann et al. 2008). Furthermore, we include an identical implementation of the basic physical processes that govern the evolution of the gaseous component in galaxy formation, such as radiative cooling and heating, star formation and feedback. Finally, we let AREPO carry out refinement and de-refinement operations on cells (if needed despite the moving mesh which normally keeps the mass per cell constant to good accuracy) in order to guarantee that the masses of cells never deviate significantly from a target given by the particle mass in the corresponding SPH comparison run. This ensures that we compare runs carried out with the two codes at about the same mass resolution.

In the last few years significant strides have been made in modeling disk galaxy formation with cosmological zoom-in simulations based on the SPH technique (e.g. Governato et al. 2010; Guedes et al. 2011). These simulations often contain millions of resolution elements per halo and incorporate feedback processes that prevent an excessive collapse of baryons into galactic components. However, these successes in reproducing properties of observed galaxies have been reached for individual halos over a limited mass range. It is not clear yet if the same model would be able to reproduce the observed population mix of galaxies over a wide range of properties. We stress, however, that our goal here is not to model galaxies with the highest possible resolution in a single system or to produce the most realistic looking galactic disks. Our comparison strategy is designed to detect systematic differences (that are projections of inaccuracies in used simulations techniques) for a large population of galaxies. While strong galactic feedback is an important component in galaxy formation and can induce large variations in the results (e.g. Scannapieco et al. 2012), we here prefer an extremely simple subresolution treatment of feedback which can be implemented numerically in a well-posed and identical way, both in our moving-mesh code and in SPH. Our strategy attempts to ensure a clean comparison by avoiding a modeling of strong feedback processes, which would significantly complicate the interpretation of differences induced by the underlying hydrodynamic technique because parameterizing such feedback in a code agnostic fashion is quite difficult.

In this Paper II of a series, we focus on an analysis of the properties of galaxies and their haloes throughout cosmic time, and discuss differences that the two simulation techniques imprint on the resulting population of galaxies. In Vogelsberger et al. (2011, hereafter Paper I), we discuss global properties of baryons in different phases, the cosmic star formation history and various code characteristics, including technical details of our updated versions of the moving-mesh code AREPO and our SPH code GADGET. Finally, in a further companion paper (Sijacki et al. 2011, hereafter Paper III) we use idealized setups of situations relevant for galaxy formation, such as gas cooling in haloes and stripping of infalling galaxies to demonstrate where and how differences between the two codes oc-

cur, which helps us to understand and interpret the differences we find in a fully cosmological environment.

We note that the conclusions reached in this paper directly apply only to standard formulations of SPH (as described, for example in Springel & Hernquist 2002). It is now well established that noisy and inaccurate pressure gradient estimates (for example see Read et al. 2010), an absence of mixing at the particle level, and comparatively large artificial viscosity lead to a number of accuracy problems in SPH, in particular a limited ability to model fluid instabilities (Agertz et al. 2007; Abel 2011) and problems in representing subsonic turbulence (Bauer & Springel 2012), which are likely the most important factors contributing to the differences we identify in this paper. We emphasise that this ‘standard SPH’ method or quite similar variants thereof have been used in the majority of the works on cosmological simulations of galaxy formation to date (both using large boxes and zoom-ins). A number of recent efforts proposed extensions or modifications of the traditional SPH formulation that aim to improve the accuracy of SPH (e.g. Wadsley et al. 2008; Price 2008; Heß & Springel 2010; Read et al. 2010; Read & Hayfield 2012; Abel 2011; Saitoh & Makino 2012). Our results do not necessarily apply to these new modified methods. They have yet to be tested for cosmological simulations of galaxy formation, and it remains to be seen whether they resolve the differences we find here in our comparison of standard SPH as implemented in GADGET3 with a more accurate hydrodynamic scheme such as the one implemented in AREPO.

The structure of this paper is as follows. In Section 2, we describe our simulation setup, the physical processes included, the initial conditions, and the most important code modifications and methods used to identify haloes and galaxies. In Section 3, we present properties of galaxies and haloes in our moving-mesh and SPH simulations. In particular, we discuss the baryon content of haloes, galaxy mass functions, gas fraction and star formation rates of haloes, disk sizes and specific angular momenta of galactic baryons. We interpret and discuss our new results from the moving-mesh cosmological hydrodynamics in Section 4.

2 METHODS

In this paper, we describe only the essential setup information for our simulations, in the interest of brevity. We refer readers to the original code papers for a detailed discussion of GADGET (Springel 2005) and AREPO (S10), as well as to Paper I for technical information about specific parameters adopted for the codes and about their relative CPU-time performance.

2.1 Simulation suite and initial conditions

We construct the initial conditions at redshift $z = 99$ and evolve them to $z = 0$, adopting the following Λ CDM cosmology: $\Omega_m = 0.27$, $\Omega_\Lambda = 0.73$, $\Omega_b = 0.045$, $\sigma_8 = 0.8$, $n_s = 0.95$ and $H_0 = 70 \text{ km s}^{-1} \text{ Mpc}^{-1}$ ($h = 0.7$). These parameters are consistent with recent WMAP-7 measurements (Komatsu et al. 2011) at the 1σ level, except for n_s which is consistent at 2σ level. The initial power spectrum was approximated with the fit of Eisenstein & Hu (1999).

Our simulation suite follows a periodic box of size $20 h^{-1} \text{ Mpc}$ at three different resolution levels: 2×128^3 , 2×256^3 and 2×512^3 particles/cells, respectively. Initially we start with an equal number of gaseous fluid elements and DM particles in both codes. While the number of DM particles stays fixed, the number

of gaseous elements changes over time. In GADGET this change owes to transformations of gas particles into star particles during star formation events, keeping the total number of baryonic resolution elements constant. Likewise, in AREPO gaseous cells turn into star particles, but occasionally can also be refined and de-refined if needed to keep the mass resolution always close to the nominal resolution present in the initial conditions. This leads to further changes in the number of cells, but overall, the total number of baryonic resolution elements stays approximately constant as well (see Paper I for more details).

We note that we have used the same random phases and amplitudes for overlapping modes on large scales for the different resolution levels, so that our simulation set can be used for a resolution study of individual objects formed in our Λ CDM realization. In Table 1, we list the symbolic names of the simulation runs, together with their principal numerical parameters, such as the initial particle/cell masses, the number of computational elements for all of our simulations, and the gravitational softening used for collisionless particles.

2.2 Gravity, cooling and star formation

The calculation of gravitational forces in all of our simulations is done with the algorithms described in Springel (2005). In short, we use a combination of a particle-mesh approach (e.g. Hockney & Eastwood 1981) to calculate large-scale forces with the help of fast Fourier transforms, and a hierarchical multipole approximation (a tree algorithm, Barnes & Hut 1986; Hernquist 1987) for short-range distances. This combination ensures a high computational speed nearly independent of the clustering state, and a uniformly high force resolution throughout the simulation volume.

For the long-range PM computation, we employ a mesh size twice as large as the corresponding particle grid, meaning that for our L20n128, L20n256 and L20n512 simulations, the mesh has 256^3 , 512^3 and 1024^3 elements, respectively. It is important to emphasize that the gravitational force calculation is done in a consistent way in AREPO and GADGET, which enables us to cleanly identify differences caused by the hydrodynamics alone. The gravitational forces are softened at small distances as described in Hernquist & Katz (1989), with the corresponding Plummer-equivalent softening length fixed in comoving coordinates at $4 h^{-1}\text{kpc}$, $2 h^{-1}\text{kpc}$ and $1 h^{-1}\text{kpc}$, respectively. These values are applied to all collisionless particles in AREPO and all particle types in GADGET. Gaseous cells in AREPO use an adaptive softening calculated as $\epsilon_{\text{gas}} = 2.5 \times (3V_{\text{cell}}/4\pi)^{1/3}$ with an imposed minimum gravitational softening length equal to the fixed softening of our corresponding GADGET simulations. However, we have also run cosmological simulations where the gas cells used a fixed softening length as well, finding that this choice does not affect the properties of galaxies found in our runs in any significant way (see also Appendix of Paper I).

We include all radiative cooling processes important for a hydrogen and helium gas of primordial composition; i.e. line cooling, free-free emission, and inverse Compton cooling off the cosmic microwave background. The rate equations are solved assuming collisional ionization equilibrium, as in Katz et al. (1996). We also include a uniform ionizing background radiation field with the normalization and time dependence of Faucher-Giguère et al. (2009) that heats and ionizes the gas in an optically thin approximation (Katz et al. 1996).

Dense star-forming gas is treated via a simple two-phase sub-resolution model as in Springel & Hernquist (2003a), which gives

rise to an effective equation of state for the dense gas. We use the same parameters for the sub-resolution model as in Springel & Hernquist (2003a), which give a threshold density for star formation of $n_h = 0.13 \text{ cm}^{-3}$. The star formation timescale scales with density as $t_* \propto \rho^{-0.5}$, and we set it to 2.1 Gyr at the threshold density in order to match the normalization of the local relation between star formation rates and gas surface density of galaxies (Kennicutt 1998). The conversion of gas mass to collisionless stellar particles proceeds stochastically based on the estimated star formation rate. We simplify the original procedure by Springel & Hernquist (2003a) further so that each gas particle spawns only one generation of stars. In addition, we modify the original model by letting gas above the star formation density threshold with a temperature higher than the effective two-phase temperature to radiatively cool in the ordinary way onto the equation of state, instead of applying the relaxation timescale of the multi-phase medium.

We note that the pressurization of the star forming medium does not drive any outflow from the galaxy. For reasons of simplicity, we do not include additional violent feedback mechanisms (e.g. galactic winds) in the present study that could significantly lower the mass of a galaxy. Our model for supernova feedback can hence be viewed as a ‘minimal feedback model’ which cannot be expected to yield a particularly realistic galaxy luminosity function, especially at the faint-end. In order to compare galaxy masses and luminosities of our predicted galaxy population with observations we will consider simulations with galactic winds in AREPO in forthcoming work. We work here with this simplified model in order to allow us to identify differences between the hydro solvers as cleanly as possible.

2.3 Cell regularization and mass homogenization in AREPO

An important aspect for the accuracy and performance of AREPO is the use of a mesh-regularization scheme that ensures a reasonable quality of the Voronoi mesh, in the sense that unfavourable cells with very high aspect ratios are avoided. As described in detail in Paper I, we have adopted a new method where cells are only regularized if the maximum angle under which a face is seen from the mesh-generating point of a cell becomes large. Regularization here means that a small velocity component towards the geometric center of a cell is added to the motion of the mesh-generating point, which is otherwise just given by the gas velocity in the cell.

In addition to the mesh regularization, we also employ on-the-fly mesh refinement and de-refinement operations, where appropriate, in order to ensure a constant mass resolution. In principle, this is not strictly required in AREPO, as the pseudo-Lagrangian nature of the scheme moves the mesh along with the mass, bringing more resolution to regions where this is needed most and maintaining roughly constant mass in cells. However, the resulting spread in mass tends to grow with time, and without explicit refinement and de-refinement measures, a relatively wide spectrum of cell masses may develop. An unwanted consequence would also be that star particles with considerable variation in mass would be created, which might lead to undesirable two-body heating effects. Therefore, we enforce cells to have a mass close to our desired target mass by splitting and merging individual cells if needed. In practice, we allow cell masses to deviate by at most a factor of ~ 2 from the desired target mass. The latter is set equal to the SPH gas particle mass in the run with the corresponding initial resolution, as listed in Table 1, so that we can ensure an equivalent mass resolution in the AREPO simulations. We note however that different refinement criteria other than mass could be chosen in AREPO,

Name	Code	Boxsize $[(h^{-1}\text{Mpc})^3]$	hydro elements	DM particles	$m_{\text{target}}/\text{SPH}[h^{-1}\text{M}_{\odot}]$	$m_{\text{DM}}[h^{-1}\text{M}_{\odot}]$	$\epsilon[h^{-1}\text{kpc}]$
A.L20n512	AREPO	20^3	512^3	512^3	7.444×10^5	3.722×10^6	1
G.L20n512	GADGET	20^3	512^3	512^3	7.444×10^5	3.722×10^6	1
A.L20n256	AREPO	20^3	256^3	256^3	5.955×10^6	2.977×10^7	2
G.L20n256	GADGET	20^3	256^3	256^3	5.955×10^6	2.977×10^7	2
A.L20n128	AREPO	20^3	128^3	128^3	4.764×10^7	2.382×10^8	4
G.L20n128	GADGET	20^3	128^3	128^3	4.764×10^7	2.382×10^8	4

Table 1. Basic parameters of our simulation set. All calculations were performed in a periodic box with side length of $20 h^{-1}\text{Mpc}$. The number of hydrodynamical resolution elements (SPH particles or Voronoi cells, respectively) becomes smaller with time due to star formation. In the AREPO simulations, additional re- and de-refinement operations are invoked to keep the cell masses close to a target gas mass m_{target} , which we set equal to the SPH particle mass of the corresponding GADGET run. The comoving Plummer-equivalent gravitational softening length ϵ is constant in GADGET, but adaptive for gas cells in AREPO.

which has a similar flexibility as AMR codes in this respect. Further details on the technical implementation of refinement and de-refinement in AREPO are provided in S10 and Paper I.

2.4 Galaxy and halo identification

We identify haloes in our simulations with the standard FOF approach (Davis et al. 1985) with a linking length of 0.2 times the mean interparticle separation. The FOF algorithm is applied only to the DM particles, whereas baryonic particles/cells are later assigned to their nearest DM particle and included in the halo to which the corresponding DM particle belongs. Self-bound concentrations of mass, termed ‘subhaloes’, are then identified within each FOF halo using the SUBFIND algorithm (Springel et al. 2001), which has recently been modified to also account correctly for baryons in subhaloes (Dolag et al. 2009).

The SUBFIND approach uses an adaptively smoothed density field (estimated from adding up the individual contributions of all particle/cell types) to find isolated overdense regions by means of an excursion set technique. Each substructure candidate identified in this way is then subjected to a gravitational unbinding procedure, leaving only the self-bound material in the subhalo. This effectively produces a list of subhaloes for each main FOF-halo. The bound part of the smooth background FOF-halo (after all embedded substructures have been removed) is defined as the ‘main subhalo’. For the centre of each FOF halo (selected as the minimum of the gravitational potential of the main subhalo) we also determine virial mass estimates with the spherical overdensity algorithm. Following a common convention in the literature, we adopt $M_{\text{halo}} = M_{200}$ as estimate of the halo mass, where M_{200} is the mass contained within a spherical region of radius R_{200} around the centre with overdensity of 200 with respect to the critical density. We use the term ‘central galaxies’ for the galaxies in the central parts of the main subhalo of a given FOF halo.

Galaxy identification can be a complex task, especially in GADGET, where a large number of cold gaseous clouds form in massive haloes at large radii (Kaufmann et al. 2009; Kereš et al. 2009a; Puchwein et al. 2010). SUBFIND tends to associate those with the central galaxies, which can skew some of their properties, like their angular momentum, half-mass radius and, in extreme cases, even their total mass. In order to protect against this effect and to make the galaxy identification closer to what would be inferred observationally, we adopt a few further criteria after subhalo identification in order to select the galactic baryons and construct the galaxy catalogue. Specifically, we assume that galaxies

include only reasonably cold gas with temperature $T < 30,000\text{ K}$, apart from the star-forming gas at high-density, whose effective temperature can be somewhat higher (due to the pressurization of the two-phase medium). We also require gas to have baryonic overdensities higher than 2000 which allows us to include all of the star forming gas but also extended gaseous disk outside of the star-forming region. Furthermore, we apply a radial cut of $r < 30\text{ kpc}/h$ comoving to both gas and stars to avoid that gaseous clouds and filaments in the outskirts of haloes, or substantial numbers of intra-group/intra-cluster stars (Puchwein et al. 2010) are included in our definition of a galaxy. While these criteria are clearly crude, they are motivated by observed properties of galaxies that contain mostly cold dense gas and stars. To exclude poorly resolved galaxies we concentrate on galaxies more massive than $256 \times m_{\text{target}}$, or when selecting by halo mass, we use $M_{200} = 256 \times m_{\text{target}} \times \Omega_m/\Omega_b$ as our adopted resolution limit.

3 RESULTS

3.1 Baryon content of haloes

In Paper I, we have shown that the dark matter halo mass functions agree very accurately between our different simulation techniques, and also converge well as a function of numerical resolution. Here we concentrate on the baryonic properties of these haloes. In Figure 1, we show the mass fraction of baryons and of gas in haloes as a function of parent halo virial mass, comparing AREPO with GADGET at different resolutions. Both fractions are expressed in units of the value Ω_b/Ω_m for the universe as a whole, which would be the expected mass ratio if the baryons would perfectly trace dark matter. Figure 1 illustrates that this is only approximately true, because the baryonic fraction is a function of halo mass and often deviates significantly from unity.

In fact, in low mass haloes below $\sim 10^{10} h^{-1}\text{M}_{\odot}$ at $z = 0$, or $\sim 5 \times 10^9 h^{-1}\text{M}_{\odot}$ at $z = 2$, the fraction of collapsed baryons is significantly lower than the universal value. This is a well known consequence of the IGM photo-heating by the UV background, effectively weakly “pre-heating” the gas, modifying the peaks in the cooling curve (Katz et al. 1996) and preventing collapse and accretion of gas into low mass haloes (e.g. Efstathiou 1992; Thoul & Weinberg 1996; Gnedin 2000). For the UV background intensity used in this paper a rapid decline in baryonic fractions is in fact expected below $\sim 5 \times 10^9 h^{-1}\text{M}_{\odot}$ at $z = 2$ and $\sim 10^{10} h^{-1}\text{M}_{\odot}$

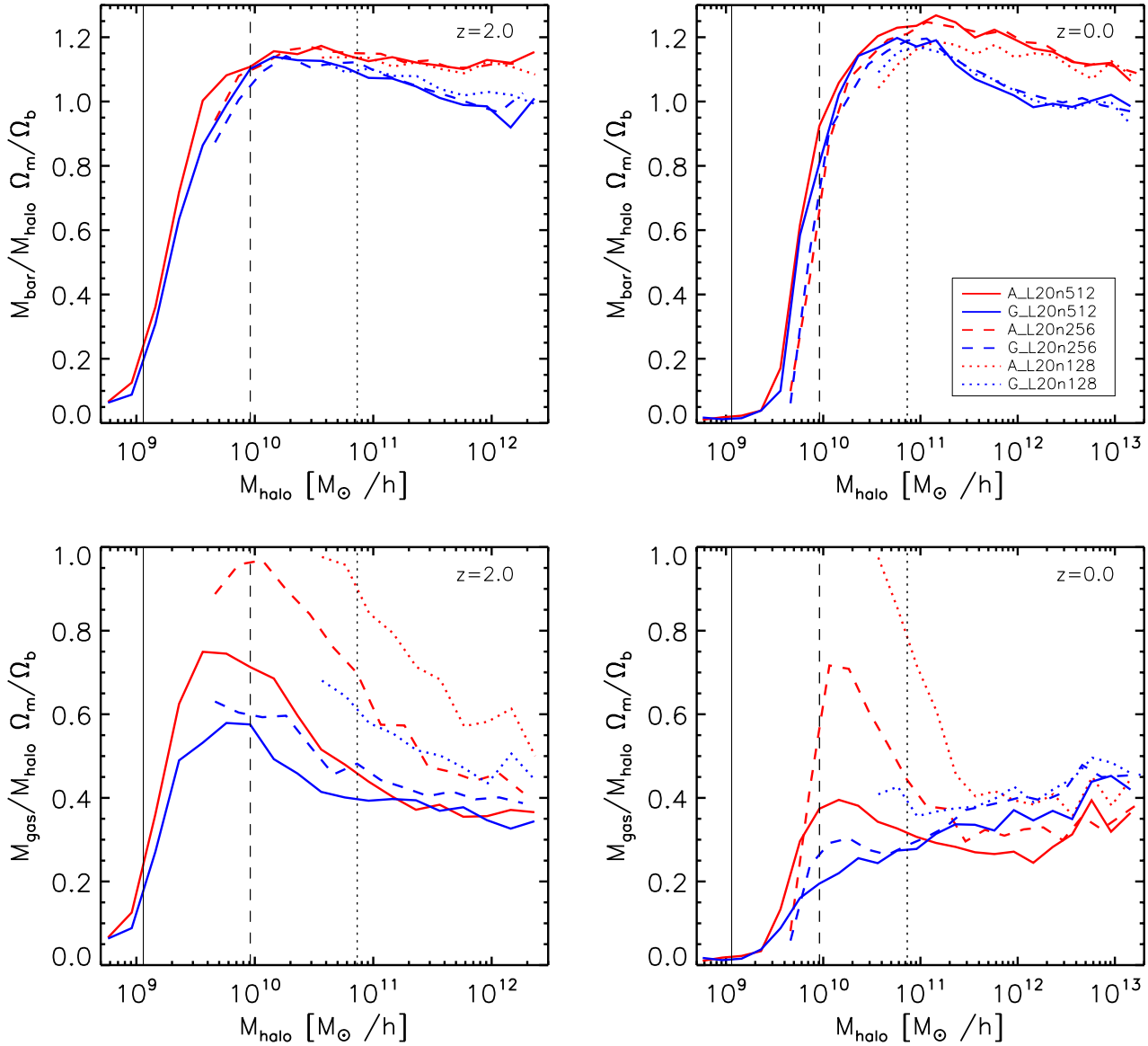


Figure 1. Baryonic content of haloes for our simulation set at $z = 2$ (left panels) and $z = 0$ (right panels). The lines show the total amount of baryons in haloes normalized by the baryon to total matter ratio in our adopted cosmology. The panels on top compare the total baryonic content in haloes of AREPO simulations (shown in red) with those in corresponding GADGET runs (blue lines). Different resolutions are displayed with different line styles, as labeled. In the bottom panels, we show the same comparison for the baryons in gaseous form (i.e. excluding stars), normalized the same way. The different vertical lines indicate a mass of $256 \times m_{\text{target}} \times \Omega_m/\Omega_b$ for each resolution.

at $z = 0$ (see also Hoesft et al. 2006; Okamoto et al. 2008; Faucher-Giguère et al. 2011). The mass scale at which haloes transition into the baryon-poor regime is consistent between SPH and AREPO and slightly increases when the resolution is poor (see the 2×128^3 runs).

More massive haloes have a baryonic content relatively close to the universal value, but with interesting trends as a function of halo mass, redshift and simulation technique. At $z = 2$, the baryonic fraction peaks 15% above the universal value at halo masses around $2 \times 10^{10} h^{-1} M_\odot$ in both codes. However, while in GADGET this drops again to about unity for $M_{\text{halo}} > 10^{12} h^{-1} M_\odot$, in AREPO there is still a baryon excess of around 10% in such massive haloes. Similarly, at $z = 0$ the peak in the baryonic fraction

has moved up a bit in halo mass scale to $\sim 10^{11} h^{-1} M_\odot$ and is even a bit higher. At this epoch, well-resolved AREPO haloes can have a 25% excess of baryons while in GADGET the peak is slightly lower. In more massive haloes, $M_{\text{halo}} > 10^{12} h^{-1} M_\odot$, the total baryon content drops again to around unity in SPH but remains around 10% higher than the universal value in AREPO. This systematic difference in massive haloes is very robust to changes in resolution. While this result may at first appear a bit puzzling, we note that such a systematic offset between the baryon fractions in SPH and mesh-based hydro codes has in fact been noticed earlier. Already the non-radiative simulations of the Santa Barbara cluster comparison project (Frenk et al. 1999) found that SPH runs had only $\sim 90\%$ of the expected baryons, whereas grid codes found a

ratio close to unity (see also O’Shea et al. 2005; Crain et al. 2007). If radiative cooling is included, simulations have been found to produce a higher baryon fraction at any given radius, including out to the virial radius (e.g. Kravtsov et al. 2005; Etori et al. 2006). Our results are thus consistent with these earlier studies, even though we find a somewhat larger difference between SPH and mesh-codes compared to Kravtsov et al. (2005) when cooling is included. Note however that our small simulation box does not probe the mass scale of galaxy clusters examined in Kravtsov et al. (2005), where the effect is likely smaller.

We speculate that the origin of the difference between SPH and the mesh codes ultimately lies in the higher dissipative heating rate we found for SPH haloes in Paper I, which effectively leads to a higher pressurization of the baryons in the gaseous atmospheres, thereby pushing them out slightly in SPH relative to the mesh-codes. When cooling is included, the baryons removed in the halo centres allow the outer gas to slide in, thereby increasing the baryon fraction inside the virial radius. Since the large AREPO haloes cool more gas, this effect is stronger in the mesh code. Also, the reduction in strength of this effect towards higher masses can be understood as a consequence of a declining cooling efficiency. In fact, when our results are extrapolated to cluster scales, they appear entirely consistent with findings in galaxy cluster simulations that include radiative cooling, and in particular, with the weak trend of a falling baryon fraction with increasing mass found there (Borgani & Kravtsov 2009). Before moving on we remark that the difference in baryon fraction also means that there is a slight but systematic difference in the virial masses of matching large haloes in AREPO simulations compared to GADGET. This difference is however $<10\%$ in most cases which means that the differences between the codes presented as bin averaged results at a given halo mass are essentially the same as they would be for binned matched samples of halos.

In the bottom panels of Figure 1, we consider the gas fractions of haloes, at redshifts $z = 2$ and $z = 0$. The gas fraction of haloes is quite low, amounting to $\sim 40\%$ of the universal baryon fraction for large haloes, implying that most of the baryons in these haloes are actually locked up in stars. In fact, in our high resolution simulations at $z = 0$ this is true for all haloes above the UV background heating limit. This extremely efficient conversion of gas into stars is a consequence of the absence of very strong feedback processes in our simulations that could eject material from the bottom of the potential well of haloes in the form of winds or superwinds. Instead, the amount of stars formed is primarily regulated by the cooling efficiency of haloes, and the differences we find between the simulation techniques reflect differences in this cooling efficiency. In particular, there is less gas in large haloes at late times in AREPO, despite the fact that these haloes contain more baryons over-all compared with GADGET. This is consistent with the stronger cooling flows and higher star formation rates we found in these objects (see also Paper I). On the other hand, in small mass systems just above the cooling threshold, AREPO retains a bit more gas, both at $z = 0$ and $z = 2$, suggesting that here the mesh code is forming stars somewhat less efficiently. In this regime, the moving-mesh code is also more sensitive to numerical resolution than SPH, showing a stronger increase in the remaining gas fraction if the resolution is degraded. As we will discuss later on in the paper, this is in part a consequence of differences in disk sizes of galaxies and the inability of low resolution simulations to resolve high density gas, both affecting the star formation efficiencies.

3.2 Galaxy mass functions

Figures 2 and 3 show galactic baryonic mass functions (stars plus gas associated with galaxies) and galactic stellar mass functions at $z = 2$ and $z = 0$ for all of our simulations. For our highest resolution simulations, the galaxy mass functions are in relatively good agreement at $z = 2$ for both simulation techniques, up to masses of several $10^{10} h^{-1} M_{\odot}$. At the high-mass end, the masses of AREPO galaxies are however systematically higher than those of GADGET galaxies, by a factor of $\sim 1.5 - 2$.

The agreement at the low mass end, is arguably to be expected. Here the galaxies accrete most of their gas rapidly with rates comparable to the gas accretion rates onto haloes (Kereš et al. 2005; Ocvirk et al. 2008). Furthermore, in this low halo-mass regime, smooth accretion dominates over growth by mergers with other galaxies (Murali et al. 2002; Kereš et al. 2005; Guo & White 2008), owing to rapid gas infall and a limited mass range available for progenitors close to the UV-background suppression mass. Therefore, there is comparatively little opportunity in these low mass haloes that differences in the treatment of hydrodynamic interactions significantly affect the growth of galaxies. However, we note that this is only approximately true as there are clearly some differences when then resolution is low, as we discuss below.

At $z = 0$, some more prominent differences become apparent. While the highest resolution simulations again show reasonably good agreement in the galaxy mass function below $2 - 3 \times 10^{10} h^{-1} M_{\odot}$, at higher masses, the differences in the galaxy mass reach a factor of ~ 2 . While both numerical methods converge to the *same* galaxy mass function at the low mass end as the resolution is improved, at the high mass end, AREPO and GADGET still converge individually, but they do so to a *different* converged result. This systematic difference manifests itself in higher galaxy masses in AREPO, which we argue is linked to a stronger cooling efficiency in massive haloes, an issue we will return to in Section 3.6.

We find that GADGET simulations show convergence in the galaxy mass function for galaxies more massive than ~ 250 baryonic particles (about $8 \times N_{\text{ngb}}$ for our runs). To compare this resolution limit to the convergence achieved with AREPO, we use vertical lines in Figures 2 and 3 to mark the mass scale that corresponds to 256 times the target cell mass. AREPO appears to converge more slowly, requiring up to ~ 5 times higher mass at $z = 2$. At $z = 0$, the resolution dependence of both codes is even stronger and the convergence of the high-resolution simulations is somewhat poorer than at $z = 2$, likely caused by differences in resolving the halo scale affected by the UV background. We caution that in the cosmological simulations without galactic outflows improved resolution always leads to a higher fraction of baryons locked up in stars, especially before reionization, as there is no efficient process to regulate formation of lower mass objects. Furthermore details of galactic structure will depend, in part, on resolution, especially since the hierarchical buildup proceeds from smaller objects that are always less well-resolved. Therefore, precise criteria for convergence depend on the galactic property one is interested in. Note also that faster convergence of SPH for some of the properties does not guarantee that it is a more accurate numerical scheme. In fact, in principle it is possible that one may even converge to a wrong result (e.g. Springel 2010b). This is because in practice once typically only increases the total particle number and spatial resolution in an SPH convergence study. However, an increase in the number of neighbours would also be needed for convergence in order to progressively beat down the SPH noise (Rasio 2000), as we discuss in detail in Paper I.

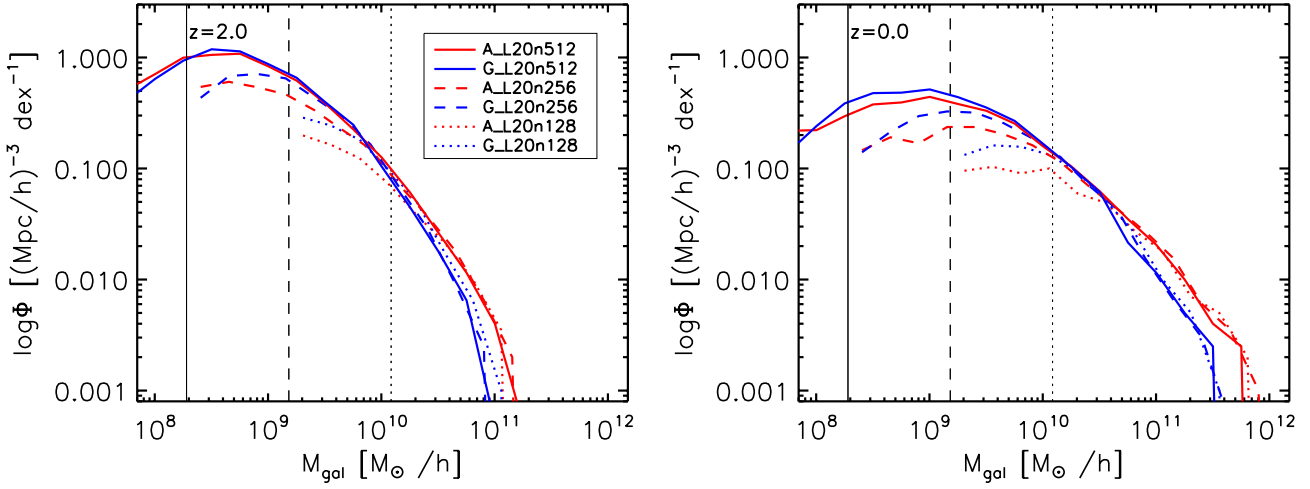


Figure 2. Baryonic mass function (gas+stars) of galaxies identified in our simulation set at $z = 2$ and $z = 0$. Runs with AREPO are shown as red lines, those with GADGET as blue lines. The different resolution levels are indicated with different line styles, as labeled. The vertical lines indicate the mass of $256 \times$ target cell/particle mass. At high redshift and at high resolution, the mass functions are similar between the codes. At $z = 0$, the differences are larger, as we discuss in the text.

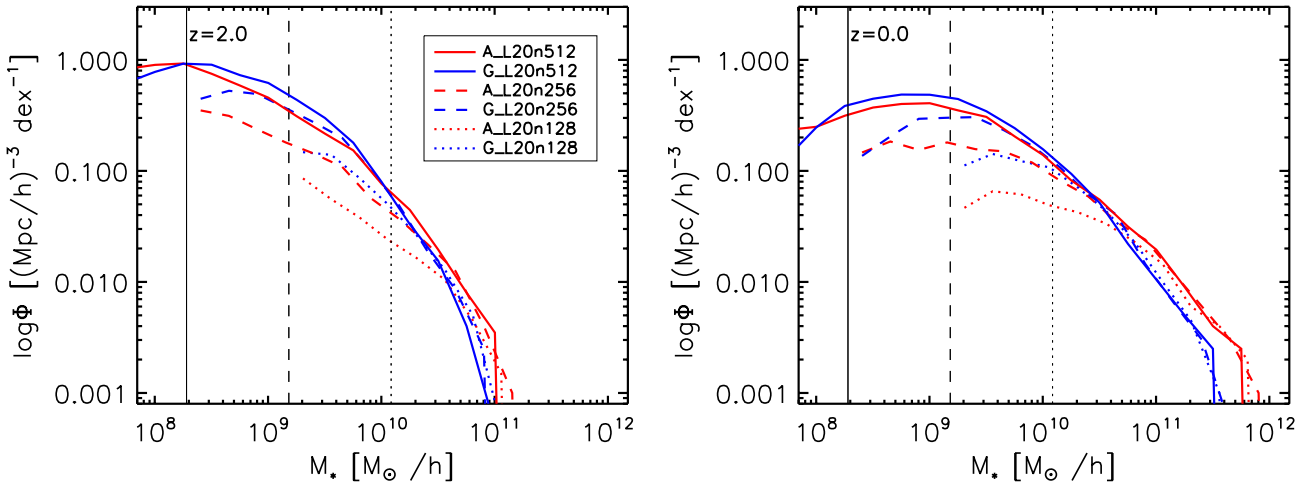


Figure 3. Stellar mass functions of galaxies for our whole set of simulations at $z = 2$ and $z = 0$. As in Figure 2, we use red lines for AREPO and blue lines for GADGET, with different line styles corresponding to different resolutions, as labeled. The vertical lines indicate a mass of $256 \times m_{\text{target}}$ for the corresponding resolution level. We note that the differences in the stellar mass function are slightly larger than the differences in the galaxy mass function, caused by systematic offsets in the gas fractions of galaxies in AREPO and GADGET simulations.

The galaxy stellar mass functions shown in Figure 3 give a qualitatively similar picture, if anything, the differences between the codes are even more evident. Here the larger offsets between the codes at low masses are caused by differences in galactic gas fractions at a given galaxy mass, as we discuss more in Section 3.4. At the high mass end, where stars form the bulk of galactic mass, a strong systematic offset in stellar masses is again clearly evident.

To summarize, while some moderate differences exist in low mass galaxies, these cannot be unambiguously attributed to systematic effects of the hydrodynamical solvers, owing to numerical resolution and galaxy finder uncertainties in this regime. On the other hand, the differences we find between the moving-mesh and

SPH codes at the massive end are very significant and robust. Here AREPO produces more massive galaxies, which is one of the key differences we will return to several times in the rest of the paper.

3.3 Relation between galaxy and halo masses

Some of the trends we inferred from the galaxy and stellar mass functions are more explicitly demonstrated in Figure 4, where we show the stellar mass and baryonic mass for central galaxies as a function of their parent halo mass M_{200} . The measurements make it clear that the agreement of the baryonic masses of galaxies in our two simulation techniques is indeed excellent in haloes of mass

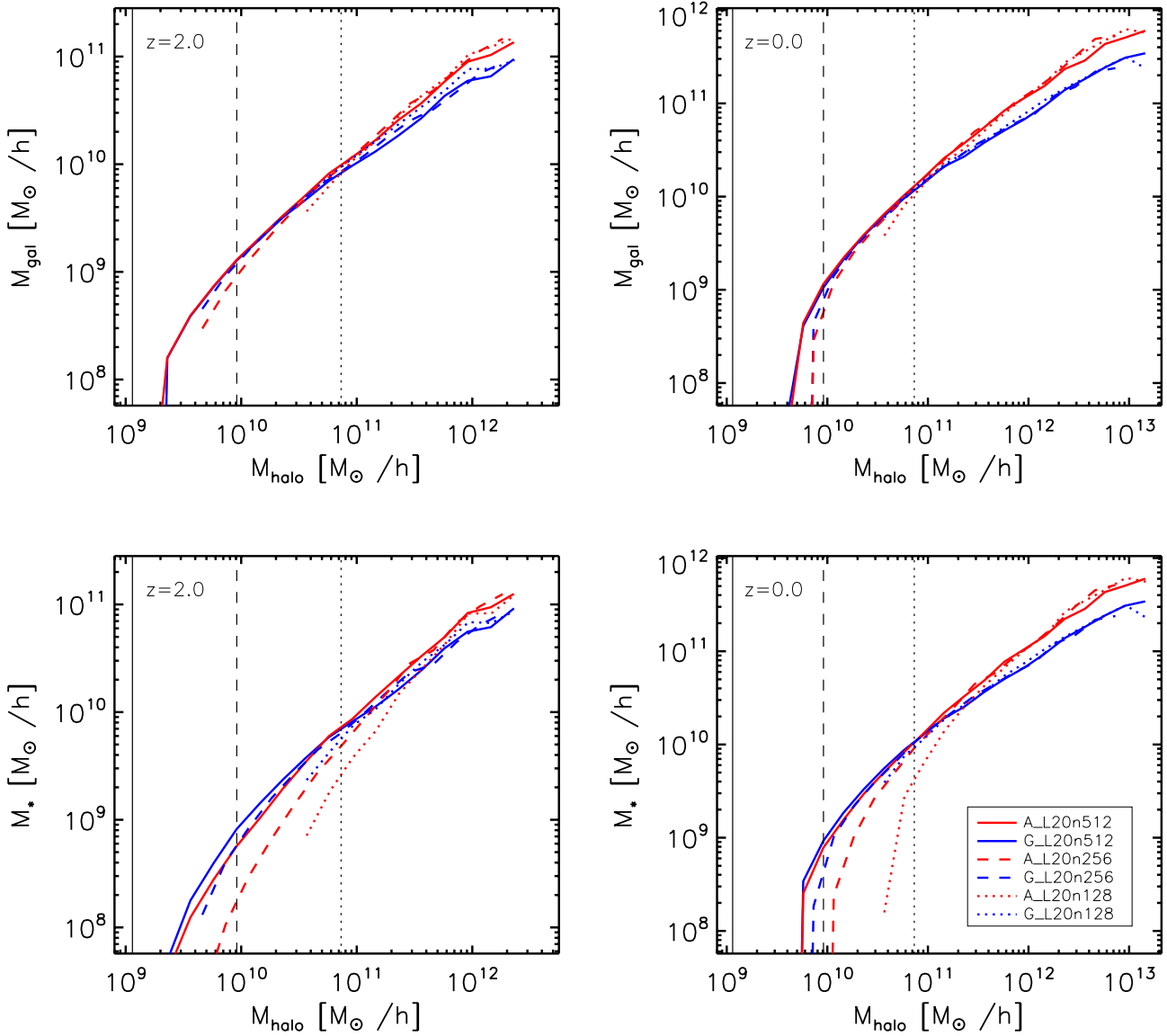


Figure 4. Dependence of galaxy and stellar mass of central galaxies on halo mass at $z = 2$ and $z = 0$. Upper panels show the galaxy mass while the lower panels show the stellar mass. We compare results for AREPO (red lines) and GADGET (blue lines) at different resolutions, as labeled. It is clear that at high resolution the galaxy masses of AREPO and GADGET galaxies are indeed very similar in haloes with $M_{\text{halo}} \lesssim 10^{11} h^{-1} M_{\odot}$, but in more massive haloes the galaxies in the moving-mesh simulations are systematically more massive. This relative mass difference increases slowly with halo mass. Vertical lines show $256m_{\text{target}} \Omega_m / \Omega_b$ at different resolutions.

$M_{200} < 10^{11} h^{-1} M_{\odot}$, whereas galaxies in more massive host haloes are systematically more massive in AREPO runs.

Because our galaxies have a relatively low gas fraction at $z = 0$, the stellar and baryonic masses are comparable at all halo masses at late times. In contrast, at $z = 2$, a lower amplitude of the stellar mass function when compared with the galaxy mass function is apparent, caused by a much higher gas content of galaxies at a given halo mass at this epoch. The differences in the galaxy masses at low resolution are more dramatic which is caused by the sharply declining masses of poorly resolved galaxies in low mass host haloes. In this case, simulations are not able to properly resolve galactic densities any more; in fact, here the gravitational softening can become comparable to the galaxy size, so that the collapse of

baryons in low mass haloes is seriously affected. We note that our findings also confirm previous results that the amount of baryons accumulated in central parts of haloes substantially exceeds the observationally inferred galaxy masses (e.g. Guo et al. 2010; Behroozi et al. 2010) if no efficient feedback mechanism is invoked that either ejects gas from these regions or somehow prevents the cooling in the first place (Kereš et al. 2009b). At the massive halo end, the AREPO simulations make this problem even more acute, strengthening the arguments for the need of very strong feedback mechanisms.

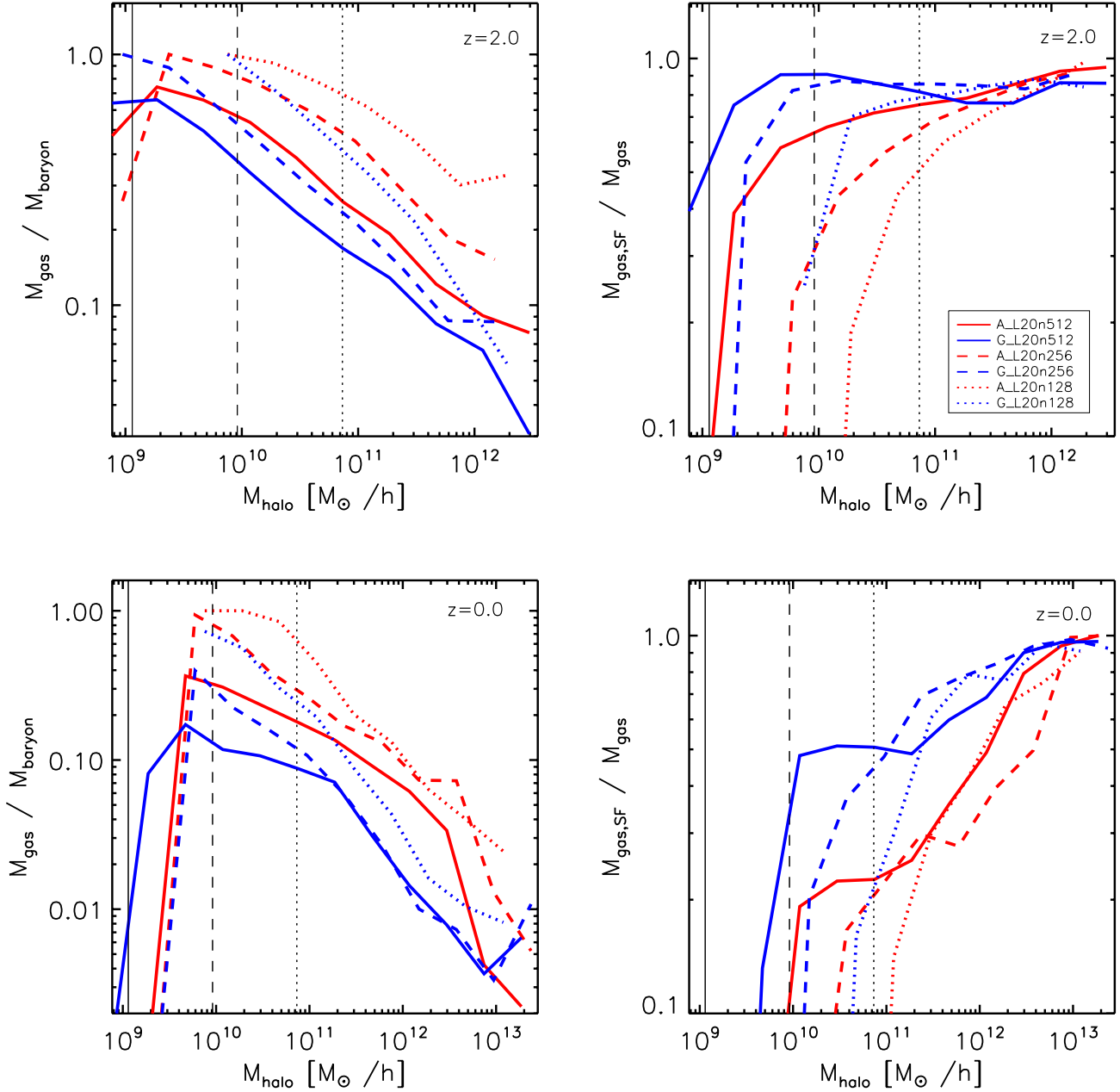


Figure 5. Gas fractions of central galaxies, $M_{\text{gas}}/M_{\text{gas}+\text{stars}}$, as a function of halo mass for our simulation set (left panels). We use red lines for AREPO and blue lines for GADGET, with different line style corresponding to different resolutions, as labeled. The gas fractions are systematically higher in AREPO than in GADGET. We also show the fractions of galactic gas that reach star-forming densities $M_{\text{SFgas}}/M_{\text{gas}}$ (right panels) to illustrate how this depends on halo mass, numerical technique and resolution. Even though both quantities are resolution dependent, the overall systematic trends clearly show higher galactic gas fractions and a lower relative fraction of gas in star-forming regions in AREPO.

3.4 Galactic gas fractions

In the left-hand panels of Figure 5, we show the gas fractions $M_{\text{gas}}/(M_{\text{gas}} + M_{\text{stars}})$ of central galaxies in our simulation runs at $z = 2$ and $z = 0$. Lines give median gas fractions at a given parent halo mass at the different resolutions. At any given resolution, the gas fractions are higher in AREPO than in GADGET runs, but the magnitude of the difference depends on the resolution of the simulation. It is interesting that even in our highest resolution

simulations, the gas fraction of AREPO galaxies are systematically higher than in GADGET indicating robust differences in galaxy evolution between the codes.

The fact that we find some resolution sensitivity is not too surprising as in our lowest resolution runs the gravitational softening can be a sizable fraction of the virial radius of low mass halo haloes and is comparable to the sizes of the corresponding galaxies. The higher resolution simulations are expected to better resolve the dense gas in galaxies, leading to a higher star formation rate, and

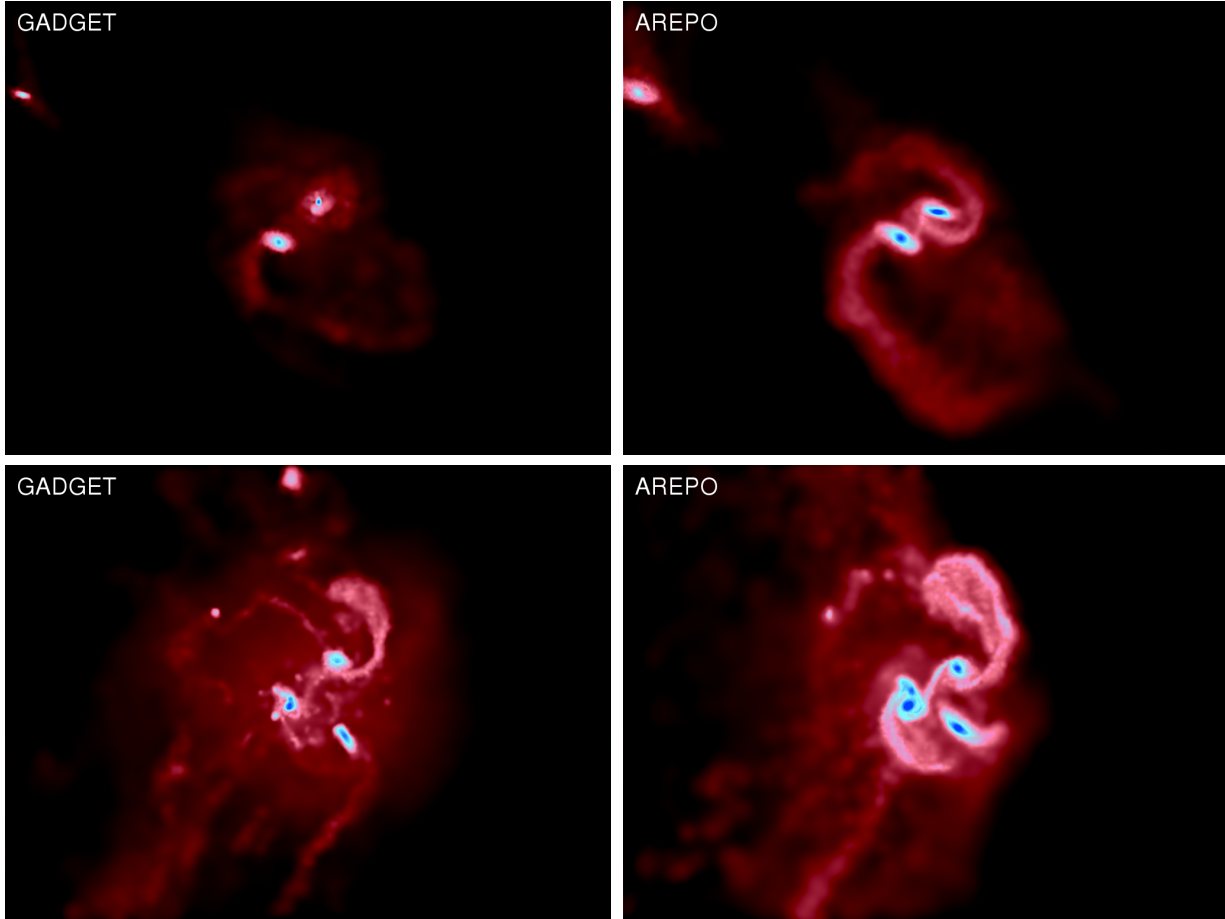


Figure 6. Projected gas distributions of two interacting galaxy systems in GADGET (left panels) and AREPO (right panels) at redshifts $z = 2$. The panels show regions of $100\text{kpc}/h$ comoving on a side. Upper panels show projections of gas in a major merger of two low mass galaxies while lower panels show a more complex merger involving three galaxies. The tidal features, tails and bridges, seen in the gas are much more prominent in AREPO, demonstrating that the galaxies simulated with the mesh code contain a larger amount of cold, rotationally supported gas.

consequently to a lower residual gas fraction at a given halo mass. Once the relevant densities are properly resolved, converged values for the gas fractions should be reached, reflecting a balance between gas supply and the depletion of gas by star formation. However, the properties of the galaxies and of their gas content will still be affected by their hierarchical formation path. The buildup of structure from quite poorly resolved small sub-components can therefore impact the gas infall rates, and also the density structure of much larger galaxies. It is hence not sufficient for convergence to achieve a sufficiently high resolution to adequately represent a given galaxy, one also needs to represent well enough a good part of the merger history leading to this object. This makes hierarchical galaxy formation a particularly difficult numerical problem.

It is clear that finite spatial resolution and the limited ability to follow the full hierarchical buildup will affect both of the codes in some ways. One might however expect numerical problems relevant to the density structure of dense galactic gas to be more severe in SPH. This is because SPH relies on an artificial viscosity in order to capture shocks and to produce the associated entropy increase. It has been shown that the artificial viscosity can lead to unwanted angular momentum transfer in the gas of a rotating galactic disk, especially when the disk is sampled with a small number of particles (Navarro & Steinmetz 1997; Okamoto et al. 2003). The net effect

is that the disk mass loses angular momentum to material further out in the halo, making these systems more compact in GADGET, resulting in turn in a faster conversion of baryons into stars and in lower residual gas fractions.

In Figure 6, projected gas densities for two different interacting galaxy systems in GADGET and AREPO are shown, supporting this picture. The tidal features, such as bridges and tails seen in the gas are prominent and well defined in AREPO, demonstrating that the galaxies simulated with the moving-mesh code contain a large amount of cold, rotationally supported gas (Toomre & Toomre 1972; D’Onghia et al. 2010). These features are much less prominent for the same systems in GADGET. This is also consistent with our findings in Section 3.7 where we show that even in low mass haloes GADGET galaxies are more compact than AREPO galaxies. We note that since poorly resolved galaxies are also the progenitors of better resolved, more massive galaxies, this effect can propagate to larger systems and induce systematic differences in them.

The gas fractions in galaxies decrease with time in all simulations, irrespective of the resolution and the code employed. The bulk of this trend is caused by a decreasing rate of gas supply into galaxies at a fixed halo mass, as commonly predicted by semi-analytic models and cosmological simulations (White & Frenk 1991; Murali et al. 2002; Hernquist & Springel 2003; Kereš et al.

2005; Dekel et al. 2009). Owing to the short (observationally motivated) star formation timescale in our ISM sub-resolution model, the rate of conversion of dense gas into stars is practically controlled by the rate of gas infall. However, this is correct only to the extent that most of the galactic gas is at high enough densities to form stars, which depends on the disk sizes. Differences in disk sizes will therefore influence the effective star formation timescale and the gas fractions. The characteristic sizes of galactic disks at a fixed halo mass increase with time (see below), enabling a larger amount of gas to reside in a disk for a given star formation rate. This slows down the evolution of the gas mass in the disk, resulting in a relatively modest drop in gas fractions with time (see also Dutton et al. 2010).

In the right-hand panels of Figure 5, we also show the fraction of galactic gas that resides in the star forming two-phase medium, i.e. $M_{\text{gas,SF}}/M_{\text{gas}}$, as a function of halo mass. At $z = 2$, in central galaxies of low mass haloes, there is more gas outside of the star forming region in AREPO than in GADGET. At $z = 0$, we find a similar difference, except for the most massive galaxies where the fraction of star-forming gas is comparable between the codes. Given that AREPO galaxies have also higher gas fractions, this implies that their galactic gas is more extended, allowing a large quantity of gas to stay below the star formation threshold. We confirm this in Section 3.7, where we demonstrate that galaxies in the moving-mesh code are more extended. It is interesting to note that in $\sim 10^{12} h^{-1} M_{\odot}$ haloes at $z = 0$ the gas fractions in AREPO are a factor of ~ 2 higher than in GADGET, even though differences in the fraction of star-forming gas are relatively minor. As it turns out these galaxies are also accreting much more gas from their surrounding hot haloes (see Section 3.6), which contributes to their higher gas fractions.

3.5 Star formation rates of simulated galaxies

In Figure 7, we show the dependence of the star formation rate of central galaxies on their parent halo mass at redshifts $z = 2$ and $z = 0$ for both codes and at three different resolutions^{*}.

The most obvious trend in Figure 7 is that the SFR is a strong function of the parent halo mass. This dependence is stronger in the case of AREPO with almost linear dependence on halo mass for the $10^{10} h^{-1} M_{\odot} < M_h < 3 \times 10^{12} h^{-1} M_{\odot}$ range. It is clear that for GADGET this relation is shallower, especially in haloes above $\sim 3 \times 10^{11} h^{-1} M_{\odot}$ where at $z = 0$ the SFR is only weakly depended on halo mass. Given the close to linear relation of galaxy mass and halo mass in Figure 4, this also implies a steep relation between SFR and galaxy mass over an extended mass range, similar to observed trends (e.g. Noeske et al. 2007; Daddi et al. 2007; Salim et al. 2007). We find that in AREPO this relation has a higher normalization and stronger dependence on halo mass at the massive end than in SPH simulations. This might help to explain the high observed star formation rates of galaxies at $z = 2 - 3$ (Förster Schreiber et al. 2009), which appear to form stars at rates higher than in previous models (Davé 2008). SFRs of simulated galaxies at a given mass show a rapid decrease with time in both codes, qualitatively consistent with observed trends and previous findings

^{*} Note that the information displayed in this figure differs from Figure 10 in Paper I by restricting the star formation measurement to the central galaxy in a halo instead of showing it summed for all galaxies within the virial radius of a halo.

from cosmological simulations (e.g. Kereš et al. 2009a; Wuyts et al. 2011).

At high redshift, GADGET galaxies show good convergence in the SFRs of large haloes, while AREPO exhibits a slightly stronger residual drift with resolution. However, for both methods, one typically finds that low resolution causes a reduction of the SFR in low-mass objects, but leads to an overestimate of the SFRs in high-mass objects. This can be understood as a generic consequence of hierarchical galaxy formation. If limited resolution suppresses some of the star formation in low-mass progenitor objects, more gas is left over to support a higher SFR in large objects once they have formed.

The SFRs in GADGET and AREPO reach similar values for low-mass parent haloes in our highest resolution simulations, which is a consequence of the relatively simple gas infall physics in this regime. However, it is clear that there is a substantial systematic difference in massive haloes where AREPO shows a much higher star formation rate in the central galaxies. The difference is especially acute for the mass range $M_{\text{halo}} \sim 5 \times 10^{11} - 3 \times 10^{12} h^{-1} M_{\odot}$ at $z = 0$, where the SFRs of central galaxies in AREPO are a factor of 3-5 times larger than for the same galaxies in GADGET. This is also the reason why the global star formation rate in AREPO is significantly higher at low redshift than in GADGET, as discussed in Paper I. Since the SFR in these massive haloes is largely regulated by the gas supply, and late-time mergers are relatively gas-poor, the main cause of these high SFRs at $z = 0$ in AREPO must lie in a more efficient cooling in massive haloes. Similar differences are apparent for masses $M_{\text{halo}} \sim 10^{12} M_{\odot}$ at $z = 2$, where AREPO's SFRs are a factor of 2-3 higher than in GADGET simulations. This is a clear example of dramatic changes in the properties of galaxies when a more accurate hydrodynamical method is used to model galaxy formation.

Interestingly, at high resolution, the SFRs of central galaxies in our most massive haloes, $M_{\text{halo}} \sim 10^{13} h^{-1} M_{\odot}$ are quite comparable between the codes and are relatively low relative to their halo mass. In the next subsection we explore the hot gas profiles in massive haloes to examine these differences more explicitly.

3.6 Gas profiles of massive haloes

In Figures 8 and 9, we show average density, temperature, entropy and radial velocity profiles of $\sim 10^{12} h^{-1} M_{\odot}$ and $\sim 10^{13} h^{-1} M_{\odot}$ haloes at $z = 0$, respectively. To measure these profiles, we first select all haloes in a narrow mass range as labeled in the temperature panels. For each halo, we find its spherically averaged profiles for non star-forming gas with $T > 10^5$ K. We then stack the haloes by finding the median value over all systems in the given mass range. This is to avoid local distortions owing to infalling substructures that often have slightly different locations in AREPO and GADGET, and hence helps to focus attention on the smooth hot halo gas only. We note that all the haloes in this mass range are dominated by the hot halo gas. To allow a more faithful stacking, we express the radius in units of R_{200} , density in terms of enclosed baryonic density within R_{200} , velocity in units of $v_{200} = \sqrt{GM_{200}/R_{200}}$ and temperature as a virial temperature, $T_{\text{vir}} = 0.5 \mu m_{\text{H}} v_{200}^2 / k_{\text{B}}$, where m_{H} is the proton mass, μ is mean molecular weight of the gas, which we here take to be fully ionized, and k_{B} is Boltzmann constant.

There are interesting systematic differences in the hot halo structure between the different simulation codes, that are especially prominent for our lower mass sample. The density profiles are steeper in AREPO compared with GADGET, showing at large radii

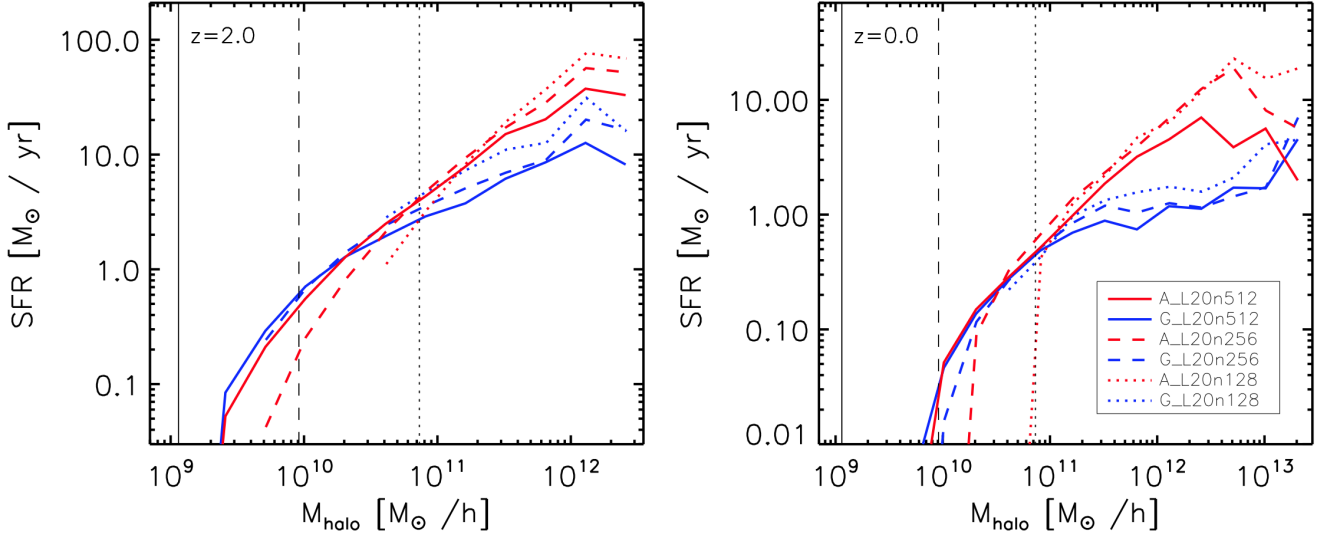


Figure 7. Star formation rates of central galaxies as a function of their parent halo mass for all of our simulations. Blue lines show GADGET galaxies while red lines show AREPO galaxies at $z = 2$ and $z = 0$. In low mass haloes in our highest resolution simulations galaxies form stars with similar rates. However in haloes more massive than $2 \times 10^{11} h^{-1} M_{\odot}$ AREPO’s star formation rates are higher at a given mass. These differences reach a factor of ~ 5 in Milky Way-mass haloes at $z = 0$. Lines show medium star formation rates at a given mass with different line types corresponding to different resolutions as labeled.

lower gas densities, and in the central parts higher density. The temperature profiles are quite similar between the two simulation techniques for $R > 0.2 R_{200}$. However, the inner region clearly shows a decrease in gas temperature in AREPO simulations indicative of a cooling flow, while the temperature continues to rise at small radii in GADGET. At lower resolution, there is an even stronger decrease in temperature and an increase in density in the innermost halo region in AREPO. Even GADGET shows some mild decline of the central temperature and a density increase, albeit with a much lower magnitude and confined to smaller radii. These density and temperature differences are reflected in corresponding trends for the entropy of the halo gas. The entropy in moving-mesh simulations is significantly higher in the halo outskirts but is lower in the central $\sim 0.1 R_{200}$ of the halo. Finally, the mean radial streaming velocity of the gas in Figure 8 shows a larger negative amplitude for AREPO than for GADGET. This can be viewed as a tell-tale sign of a larger cooling rate out of the AREPO haloes.

These trends provide a clear explanation for the large differences in SFRs between the two simulation techniques visible in Figure 7, which are induced by a much more efficient cooling in haloes with mass $\sim 10^{12} h^{-1} M_{\odot}$ in AREPO. In the more massive, group-sized haloes shown in Figure 9, the differences between the gas profiles are however much smaller. There are still similar trends of a lower gas density in the outskirts and higher densities and lower entropies in the central parts of AREPO haloes that indicate some residual cooling difference. However, the temperature profiles are very similar between the codes, except for a slightly steeper rise of the central temperatures in the moving-mesh approach, which is likely caused by a deeper potential well owing to a much higher accumulation of baryons in the centre. Also, in both codes the central entropy remains relatively high and the central temperature does not show signs of strong cooling. This explains the relative low SFRs over this halo mass range and the relative consistency between AREPO and GADGET. The long cooling times are also reflected in the radial infall profile, which shows that the

hot halo gas is essentially in hydrostatic support and has very little average motion in the radial direction. We note that the high entropies in massive haloes in GADGET are consistent with previous results from cosmological simulations with cooling and star formation (Kereš et al. 2009a), but interestingly, the trend we find here between AREPO and GADGET is opposite to what is typically found in non-radiative simulations of cluster formation where the central entropies of massive haloes are found to be higher in mesh codes (Frenk et al. 1999).

Interestingly, we also find that the acceleration profiles due to hydrodynamical pressure forces ($-\nabla P/\rho$) are very similar between the two codes, as expected for the same haloes in quasi hydrostatic equilibrium, because the pressure forces need to balance gravity, which is dominated by the same dark matter distribution in both codes. It is then at first a bit puzzling to understand why the AREPO haloes are cooling more gas than GADGET, as is clearly evident by the significantly different radial streaming velocities. While the lower central temperatures and higher central densities in AREPO may suggest a higher cooling rate overall, note that this is really only the case in the innermost regions of the haloes, but much of the volume and gas mass of the haloes sit at larger radii. There, the gas density in AREPO is actually comparable or slightly lower than in GADGET, as is also expected due to the reduced remaining gas content we have measured for these haloes in AREPO at late times (because more stars have been formed). This means that the total energy losses from emitted cooling radiation are actually quite comparable for the two codes, especially in the relevant region around the cooling radius in the outer parts of the haloes. Given these cooling losses, the surprising thing is then actually not that AREPO cools out so much gas, it is that GADGET cools out so little gas, especially in $\sim 10^{12} h^{-1} M_{\odot}$ haloes where the cooling times are short.

We argue that this is due to the difference in dissipative heating between the two codes that we measure for such quasi-stationary haloes in Paper I. In SPH, a combination of viscous dissipation

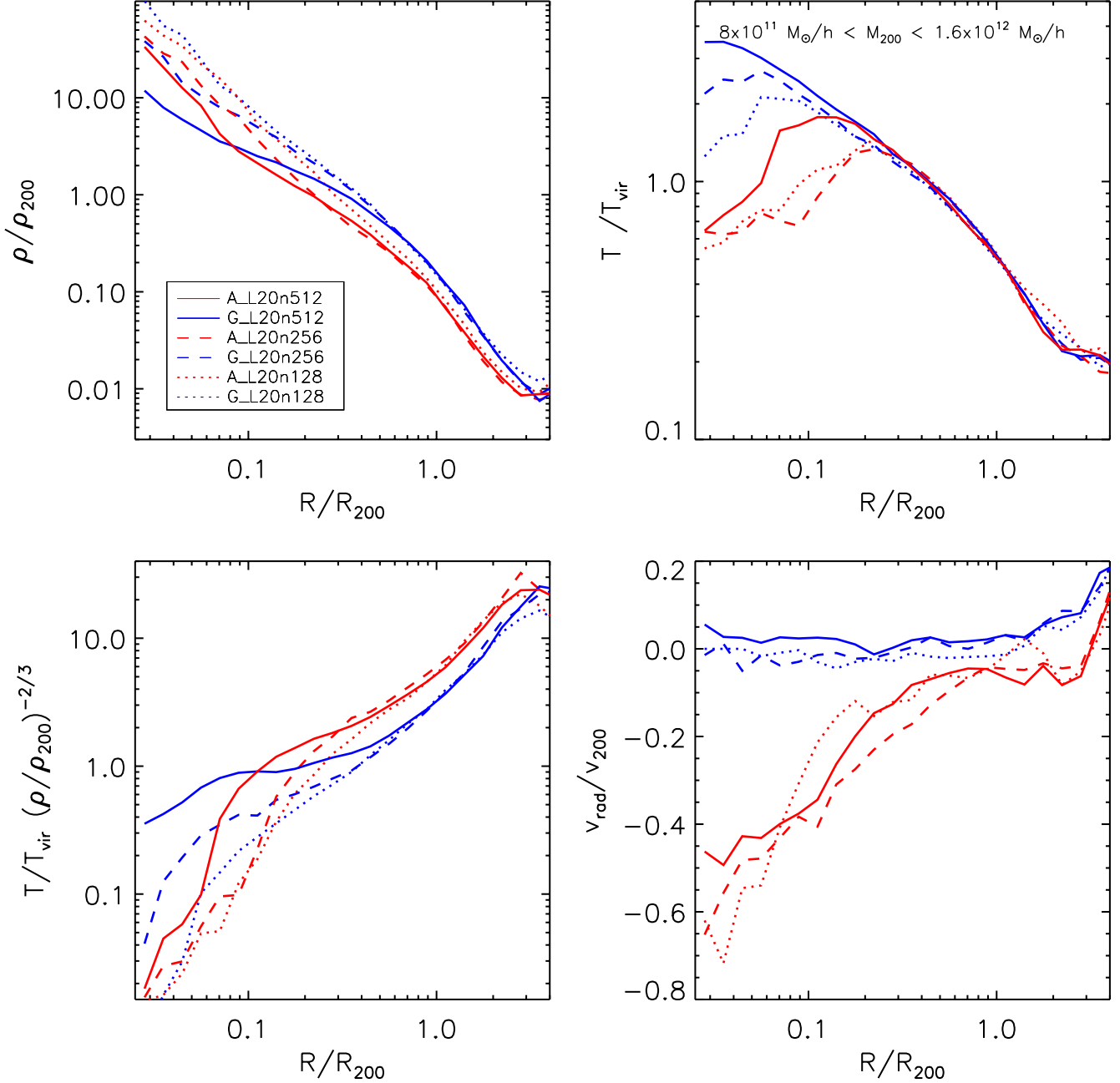


Figure 8. Density, temperature, entropy and radial velocity profiles of $\sim 10^{12} h^{-1} M_{\odot}$ haloes at $z = 0$. We only include gas that is outside the two-phase star-forming medium and has temperature $T > 100,000$ K, in order to concentrate on properties of hot halo gas. The radius is expressed in units of the virial radius (R_{200}), temperature is scaled to the virial temperature, density is expressed in units of the mean enclosed baryonic density of our haloes, ρ_{200} , and velocity is scaled to the circular velocity at R_{200} . Red and blue lines are for haloes simulated with AREPO and GADGET, respectively, while different line styles indicate different numerical resolutions, as labeled in the density panel. The halo mass range stacked for the measurements is given in the temperature panel and includes between 14 and 20 haloes.

of sonic velocity noise of the gas and efficient damping of turbulent gas motions injected in the infall regions leads to a significant heating of the outer parts of haloes, partially offsetting the cooling losses there. In contrast, AREPO produces less dissipative heating in this region, so that a stronger cooling flow and higher radial infall velocities result. The adiabatic heating of the gas on its way inward is then maintaining roughly constant or even rising temperatures for the gas, despite the cooling, until it eventually drops cata-

trophically in temperature at very small radius, and is then rapidly flowing onto the star-forming phase. In addition, stripping of more gas-rich disks in AREPO and subsequent mixing of this low-entropy material (which is suppressed in GADGET) can further strengthen cooling in the central region of AREPO haloes.

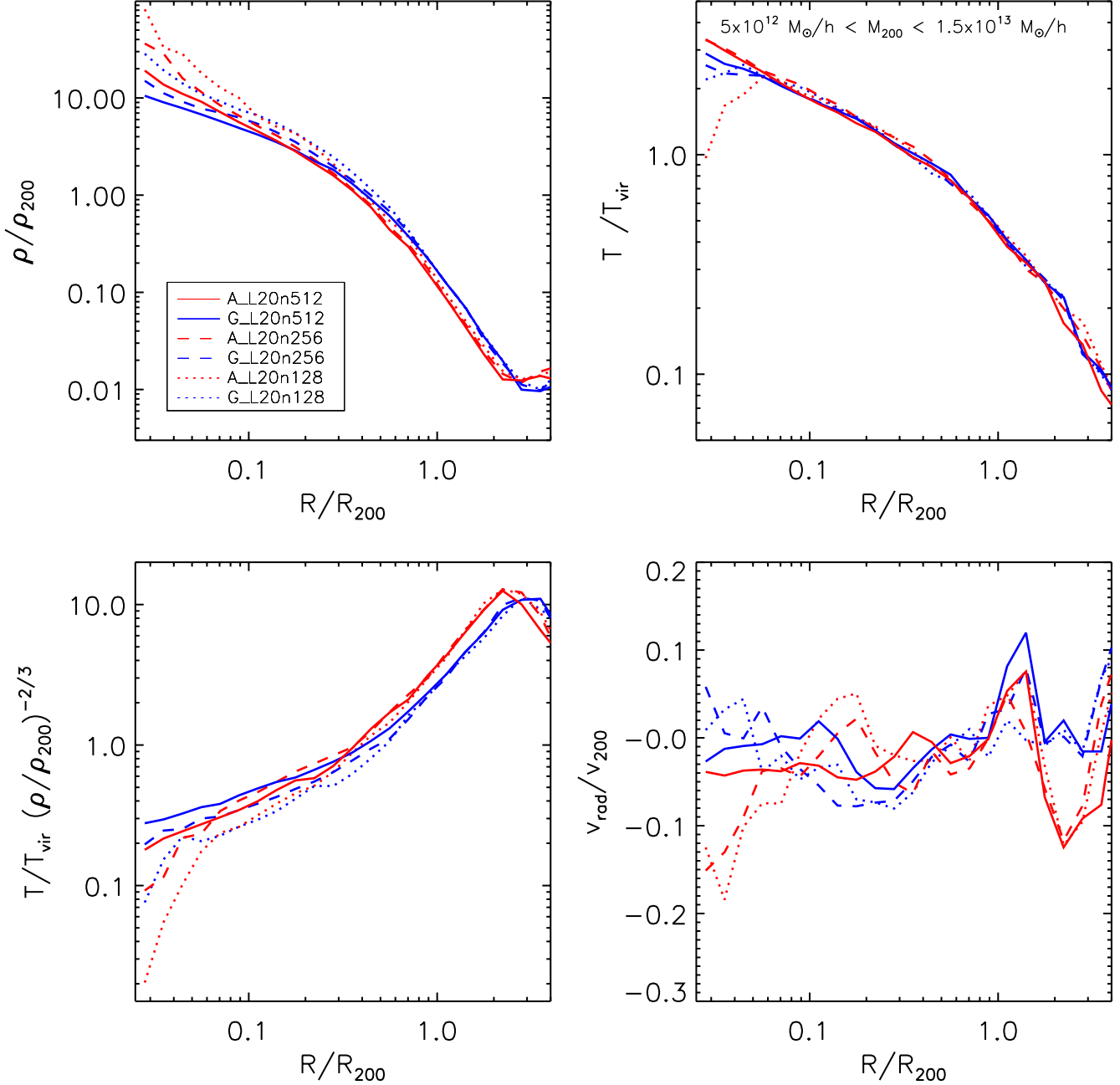


Figure 9. Density, temperature, entropy and radial velocity profiles of $\sim 10^{13} h^{-1} M_{\odot}$ haloes at $z = 0$. The selection criteria for the gas and the units chosen are as in Figure 8. The halo mass range used for the stacking is stated in the temperature panel and contains 5-6 haloes.

3.7 Characteristic size and specific angular momentum of galaxies

As an illustration of differences in the sizes and shapes of galaxies, we compare in Figure 10 the gaseous and stellar morphology of a typical late-type galaxy formed by our two simulation codes. Each projection shows the gas or stellar mass density within a box of physical side-length $50 h^{-1} \text{ kpc}$ centered on the galaxy. The galaxy shown is one of the most massive galaxies in our simulated volume at $z = 2$, and the same object was selected for a discussion of its large-scale environment in Paper I.

The galaxy resides in a halo of mass $M_{\text{halo}} \sim 9.1 \times$

$10^{11} h^{-1} M_{\odot}$, and its most important quantitative measurements are summarized in Table 2. The visual impression already indicates that the galaxy is more massive, more extended and has a much higher gas fraction in AREPO, which is born out by our quantitative measurements. In fact, the star formation rate is a factor of ~ 2 higher in AREPO than in GADGET, illustrating the principal difference between the codes we discussed in the previous sections. In addition, the gaseous disk is clearly much more extended in AREPO, as well as being thinner and more well-defined. While the difference in the half-mass radius is $\leq 60\%$, the net specific

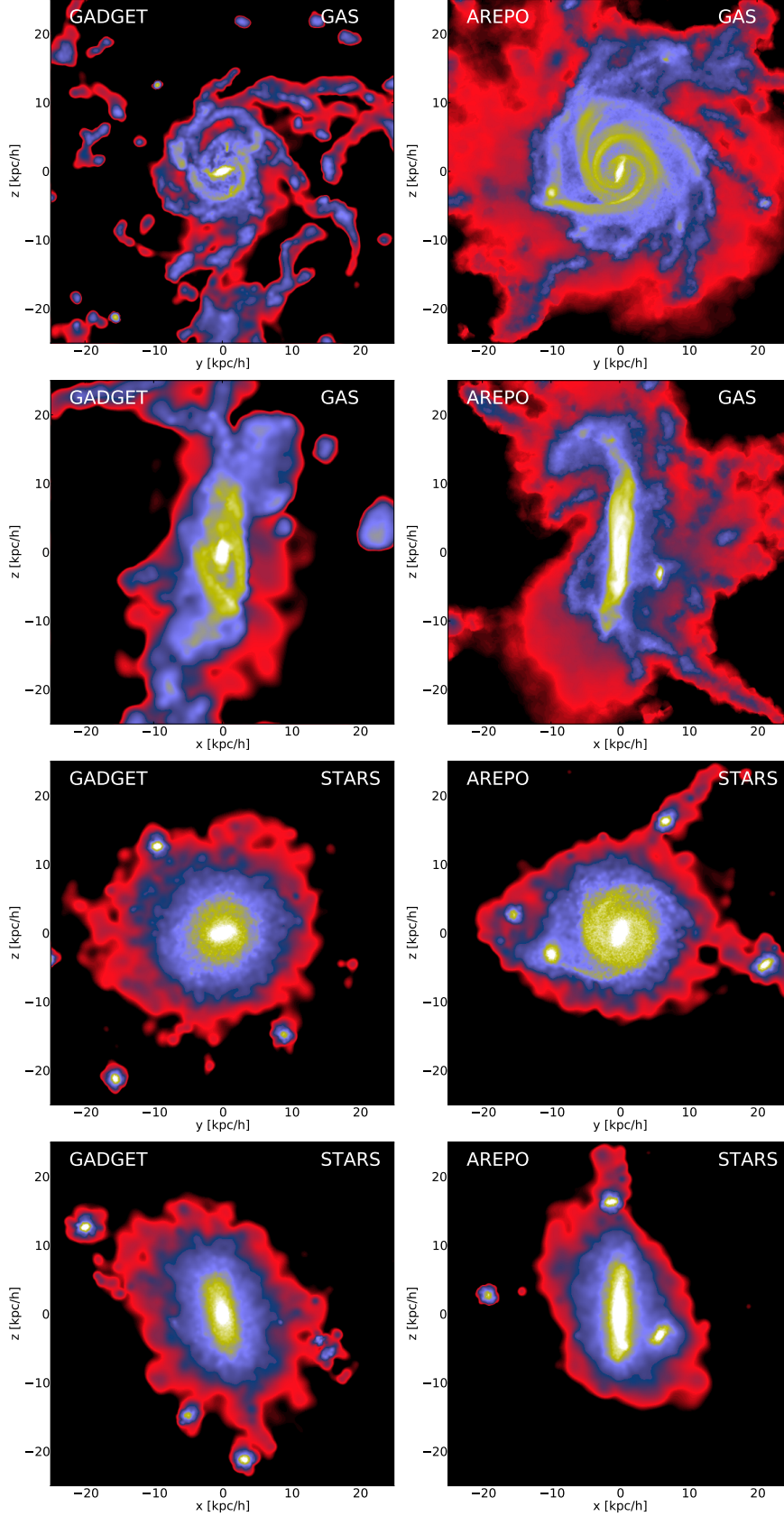


Figure 10. Example of a massive disk galaxy at redshift $z = 2$ in AREPO and GADGET L20n512 simulations. The upper two rows of panels show the projected surface density of gas in a $50 h^{-1} \text{kpc}$ physical box centered on the galaxy for two different lines-of-sight. The galaxy is clearly more extended in AREPO and has a smoother distribution of dense gas. Some quantitative properties of the object are summarized in Table 2. The edge-on projection in AREPO reveals a structure that looks more disk-like. The lower two rows of panels show projected stellar surface density in the same volume and for the same lines-of-sight. Clearly, also the stellar component of this large galaxy has a more disk-like morphology in AREPO compared with GADGET. Note that gaseous and stellar disks in the edge-on projection exhibit higher degree of alignment in the moving-mesh code.

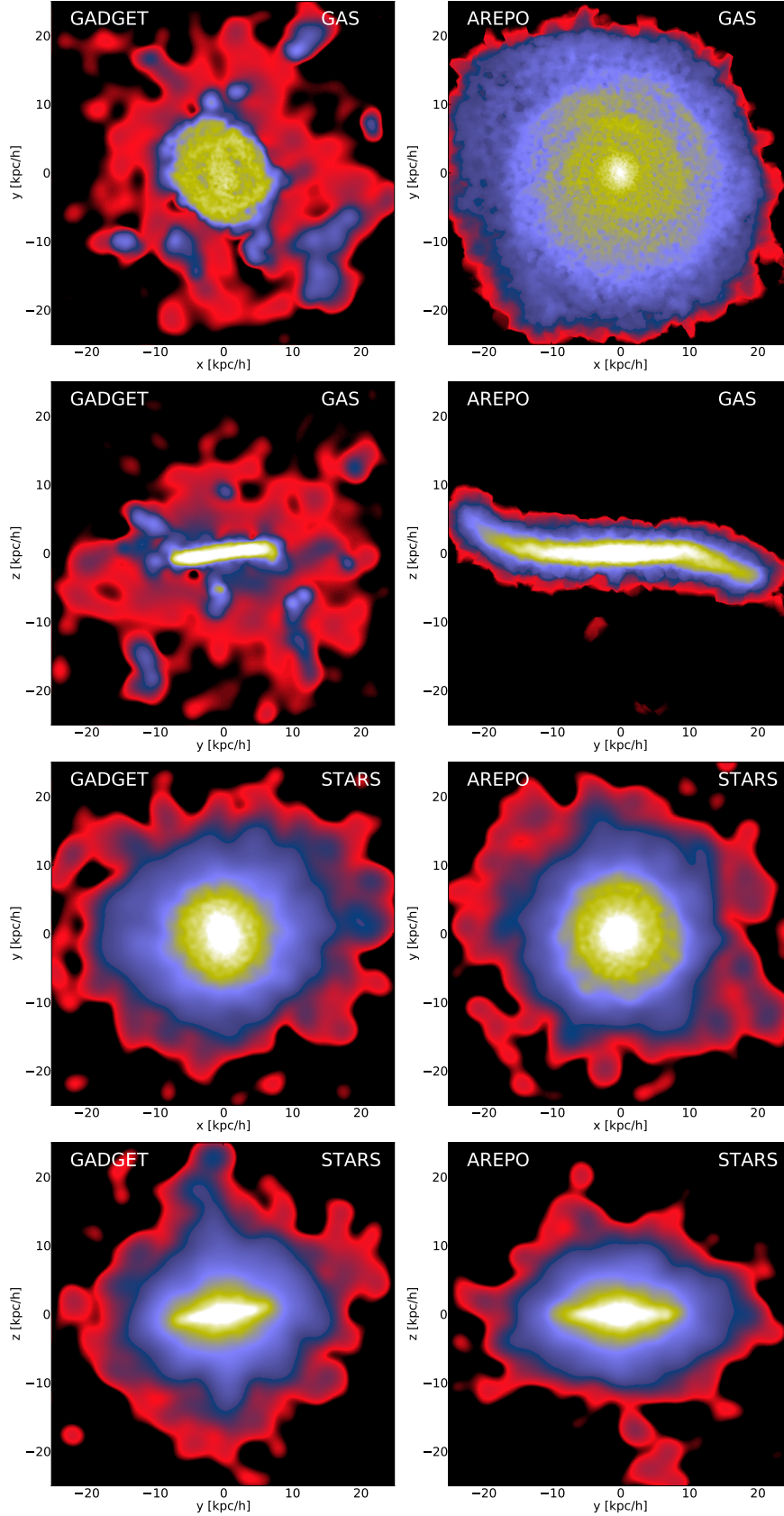


Figure 11. Example of a disk galaxy at redshift $z = 0$ in AREPO and GADGET L20n512 simulations. The upper two rows of panels show the projected surface density of gas in a $50 h^{-1} \text{kpc}$ physical box centered on the galaxy for two different lines-of-sight. The galaxy is clearly more extended in AREPO and has a smoother distribution of dense gas. Some quantitative properties of the object are summarized in Table 2. The edge-on projection in AREPO reveals a structure that looks more disk-like. The lower two rows of panels show projected stellar surface density in the same volume and for the same lines-of-sight. The stellar component of this large galaxy also has a more disk-like morphology in AREPO compared with GADGET.

Code	M_{gal} [$10^{10} h^{-1} M_{\odot}$]	M_{gas} [$10^{10} h^{-1} M_{\odot}$]	$r_{1/2 \text{ gas}}$ [$h^{-1} \text{kpc}$]	SFR [$M_{\odot} \text{ yr}^{-1}$]	j_{gas} [$h^{-1} \text{km s}^{-1} \text{kpc}$]	j_{star} [$h^{-1} \text{km s}^{-1} \text{kpc}$]	Angle [$^{\circ}$]
<i>z = 2 Example</i>							
A.L20n512	12.88	2.03	5.91	37	2108	573	7
G.L20n512	7.56	0.60	3.75	18	1150	352	18
<i>z = 0 Example</i>							
A.L20n512	3.35	0.75	10.1	1.3	1576	285	5
G.L20n512	2.2	0.24	5.3	1.4	817	218	10

Table 2. Properties of the example galaxies shown in Figures 10 and 11 as measured in our L20n512 simulations. In column (1) we list the simulation name, column (2) gives the galaxy baryonic mass, and column (3) the gas mass of our selected galaxy. In column (4) we give the effective half-mass radius of gaseous disk in physical units. Column (5) indicates the star formation rate of this galaxy, while columns (6) and (7) give the specific angular momentum of gas and stars. We note that this galaxy has a much higher gas fraction, gas extension and a higher star formation rate in AREPO than in GADGET, which is a typical systematic difference we find for massive galaxies between the codes.

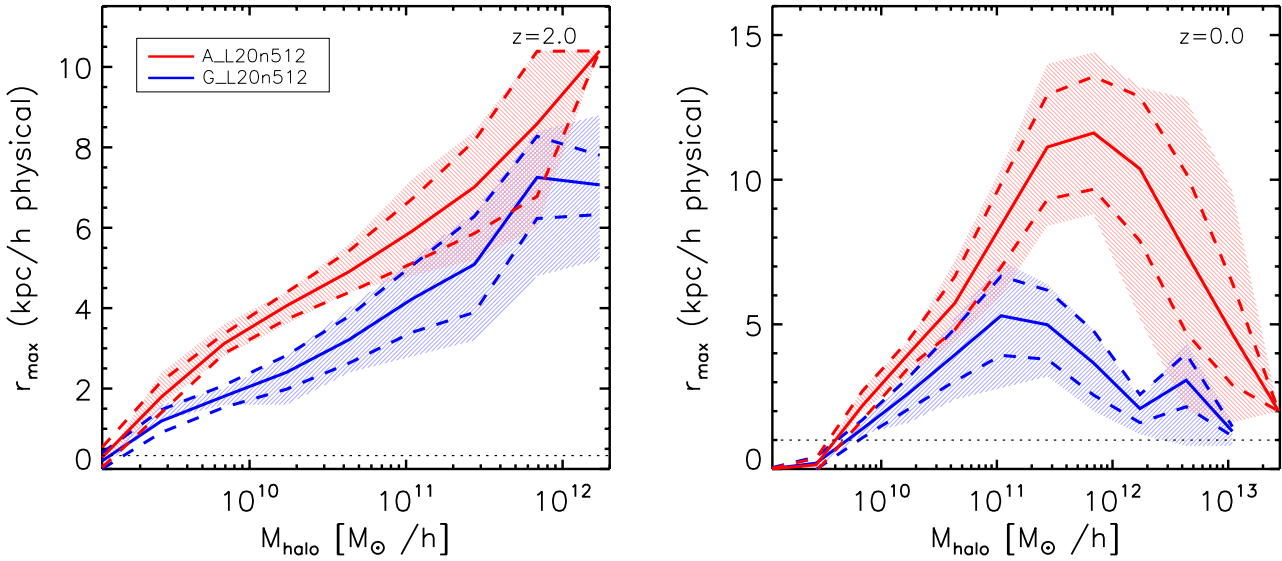


Figure 12. Dependence of the size of gaseous disks of central galaxies in GADGET and AREPO simulations on the parent halo mass (for a bins size of 0.4 dex in halo mass). The solid lines show the average “edge” radius of the dense gaseous disk, i.e. the largest radius within which the azimuthally averaged column density of cold dense gas projected onto the disk plane is greater than $N_H = 2 \times 10^{20} \text{cm}^{-2}$. Shaded regions show the 25-75% range of the distribution of disk sizes at a given mass, while the dashed lines indicate the standard deviation around the mean. It is apparent that the dense, continuous gaseous disks in AREPO are much more extended than their counterparts in GADGET. This holds at all halo masses, both at $z = 2$ and $z = 0$, and it is most dramatic in haloes around $10^{12} h^{-1} M_{\odot}$ at $z = 0$.

angular momentum of the gaseous disk is almost 2 times larger in AREPO than for the same galaxy in GADGET.

Similarly, the stellar disk is somewhat more extended and thinner in AREPO, as seen in Figure 10. It also has a higher rotational support, as indicated by the net stellar specific angular momentum which is about 60% higher in AREPO compared to GADGET. This is consistent with the visual impression of a more disk-like stellar distribution in AREPO. It is also evident that the stellar and gaseous disks are better aligned in AREPO, as measured by the angle between the angular momenta of gas and stars in the galaxy. We note that our findings in this halo represent typical differences in the properties of massive galaxies, and are by no means restricted to a single system.

Figure 11 shows another example of extended gaseous disk, this time of a central galaxy in $\sim 2.2 \times 10^{11} h^{-1} M_{\odot}$ halo at $z = 0$.

The figure demonstrates that gaseous disks are even more extended at late times and the relative difference between AREPO and GADGET is now even larger. The example galaxy contains 3 times more gas in its large disk, most of which is non-star forming and represents a large extended gaseous reservoir. Galactic interactions between such disks can lead to strong, extended tidal features such as the ones visible in Figure 6, while compact gaseous disks of GADGET galaxies are unlikely to produce them in cosmological simulations. Differences in the stellar distribution are visible in the bottom panels of Figure 11 with the galaxy appearing more disk-like in AREPO as a consequence of higher specific angular momentum of stars in our moving-mesh simulation (see Table 2). This galaxy, however, does show a large bulge component that is similar in both simulations (and is a fairly typical example for this halo mass), suggesting the need for an efficient feedback mechanism that can re-

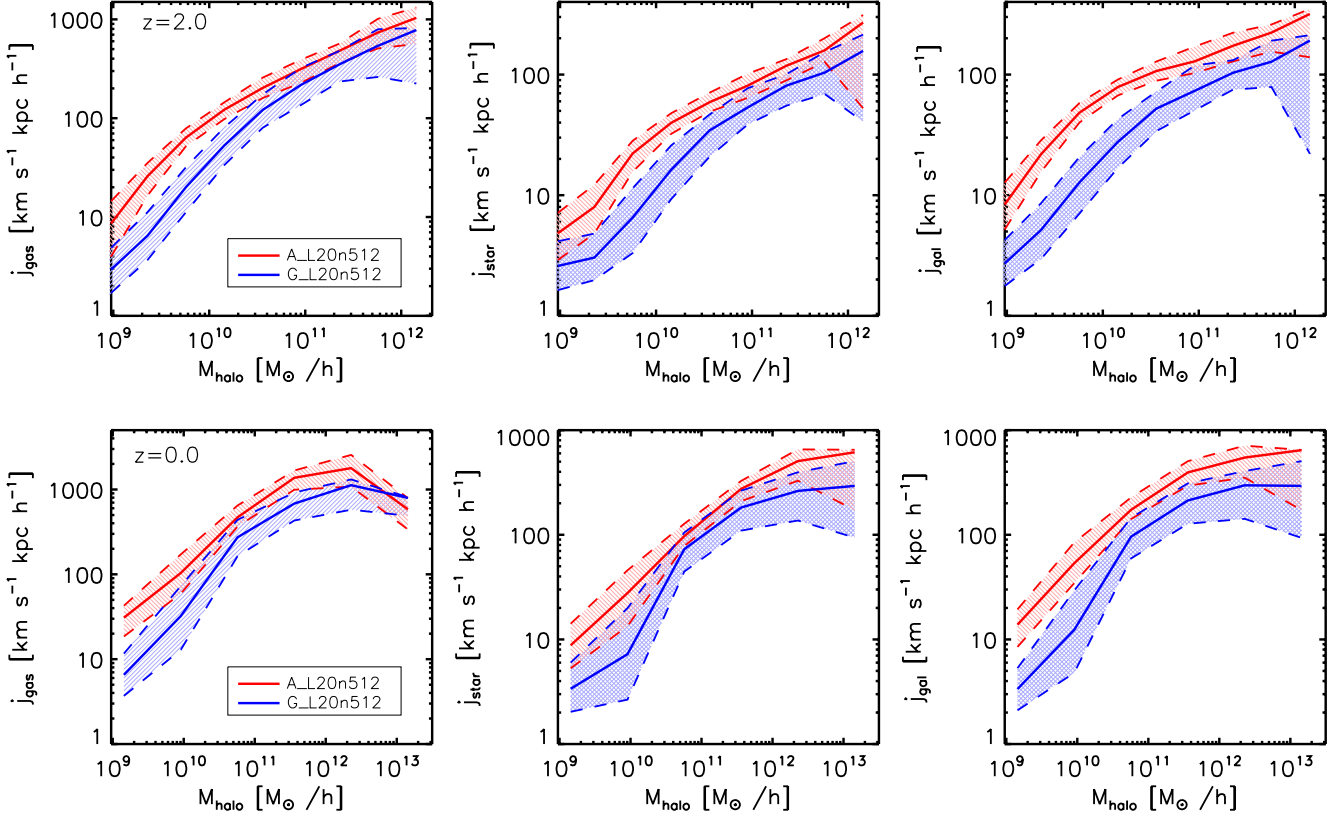


Figure 13. Specific angular momentum of galactic gas (left panels), galactic stars (middle panel) and for the whole galaxies (right panels), at $z = 2$ and $z = 0$, as a function of the parent halo mass. The measurements demonstrate that in AREPO (red lines) both the gaseous and stellar components have a higher specific angular momentum than in GADGET (blue lines), indicating diskier, more rotationally supported baryonic configurations. Shaded regions and corresponding dashed lines show 25-75% of the angular momentum distribution in a 0.4 dex mass bin at $z = 2$, and 0.8 dex mass bin at $z = 0$.

move a large fraction of low-angular momentum baryons (e.g. van den Bosch 2001; Maller & Dekel 2002; Brook et al. 2011).

In order to demonstrate this point more systematically we show a measure of the extent of gaseous disks in our highest resolution simulations in Figure 12. For this purpose we project the mass of cold, dense gas onto the gaseous disk plane of a central galaxy. Next, we find the azimuthally averaged surface density of the cold, dense gas in 0.4 kpc wide rings. We define “disk radius” as the radius at which the ring-averaged column density drops to a column density characteristic of damped Lyman- α absorbers, $N_H = 2 \times 10^{20} \text{ cm}^{-2}$. From the results in Figure 12 it is clear that galaxies in our high-resolution AREPO simulation are much more extended than galaxies in GADGET. At $z = 2$, the difference in the average extent of gaseous disks is typically around a factor of ~ 1.5 while for the most compact galaxies it is closer to factor of ~ 2 . In addition, visual inspection indicates that the disks in AREPO are not only more extended but are also smoother, thinner in edge-on projections and have better aligned gas at different radii (as visible in Figure 10). This makes their appearance more similar to the observed galactic disks. In contrast, GADGET galaxies show a more irregular gas distribution in the disk, and numerous dense gaseous clumps in the galactic surroundings.

At $z = 0$, below a halo mass of $10^{11} h^{-1} M_\odot$, AREPO galaxies are also a factor of ~ 1.5 larger, but in more massive haloes the size difference is even more dramatic than at $z = 2$. For about an order of magnitude in halo mass around $10^{12} h^{-1} M_\odot$, galaxies formed

in our moving-mesh simulations are systematically larger than in SPH by a factor of 3-5. Notice that this is a mass range of great interest as it corresponds to the halo masses of massive late-type disk galaxies such as our own Milky Way.

The measurement of gas disk sizes, as shown in Figure 12, has been specifically chosen to capture as closely as possible visual impressions from Figure 10 and 11 (see also Figures 2 and 4 in Paper I). The trends of Figure 12 are fully consistent with a more in depth analysis presented in Torrey et al. (2011), which is based on detailed Sersic and exponential disk profile fits. We note that stellar half-mass radii are only barely resolved even in our highest resolution simulations, being of the order of 1 – 3 times the gravitational softening length. We can therefore not make definitive statements about the radial extent of the stellar component, based on a rather coarse diagnostic such as half-mass radii. Nonetheless, the full extent of the stellar component is well resolved in our simulations and can be used to infer at least some of the stellar disk properties, such as total angular momentum (see below).

To characterize the degree of orderly rotation of stellar and gaseous components of galaxies we calculate the angular momentum of individual gas cells/particles and stellar particles with respect to the galaxy center and find the total angular momentum vectors for gas and stars in a galaxy. We normalize this by the gaseous and stellar galaxy mass, respectively, before calculating the magnitude of the net specific angular momentum. We apply the same procedure for the galaxy as a whole. The results are shown in Fig-

ure 13 in terms of the net specific angular momenta of gas, stars and total baryons (gas+stars) in galaxies in our highest resolution simulations. Not too surprisingly, for the cold, dense galactic gas, the structural differences we have observed earlier in the characteristic radii are also reflected in the specific angular momentum of the galactic gas, which is higher in AREPO than in GADGET by a factor of ~ 2 , explaining the larger sizes of galaxies forming in our moving-mesh simulations.

Substantial differences are also visible in the distribution of the stellar specific angular momentum shown in Figure 13. Because galaxies in AREPO are diskier, their specific angular momentum is much higher than in GADGET galaxies. This statement applies to both $z = 2$ and $z = 0$, with typical angular momentum differences at $10^{12} h^{-1} M_{\odot}$ of the order of $1.5 - 2$.

In Figure 13, we also indicate the spread of the distribution in specific angular momentum by indicating the 25% and 75% percentiles of the distribution at a given mass. The distribution of specific angular momentum at a given mass is much narrower in AREPO than in GADGET. In terms of specific angular momentum of both gas and stars in the $10^9 - 10^{12} h^{-1} M_{\odot}$ mass range, there is very little overlap between galaxies in AREPO and GADGET. For example, galaxies within the lowest 25% of the distribution in AREPO often have similar specific angular momentum as the top 25% of galaxies in GADGET.

Interestingly, the differences between the net specific angular momentum for the total baryonic content of galaxies are even larger than for the stellar content, where AREPO galaxies have up to a factor of ~ 2 higher specific angular momentum than GADGET galaxies. This results from a combination of higher gas content and higher net specific angular momentum in AREPO, and a better alignment of the gaseous and stellar components.

In our measurements, we see a trend of an increase of the gaseous disk extent and the specific angular momentum of galaxies with halo mass and time. Both effects are consistent with expectations of simple models of the formation of galactic disks (Fall & Efstathiou 1980; Mo et al. 1998; Somerville et al. 2008). In fact, these trends are qualitatively easily understood in the inside-out model of disk formation (Fall & Efstathiou 1980) where the galaxy sizes will approximately scale like $R_d \propto \lambda R_{\text{vir}}$, where λ is the dimensionless spin parameter (Peebles 1969) and R_d is the disk scale length. The specific angular momentum then approximately scales as $j \propto \lambda \times R_{\text{vir}} \times V_c$. Because the spin parameter is approximately independent of mass and redshift (e.g. Barnes & Efstathiou 1987), the sizes and specific angular momenta of galactic gas both increase with time and mass. Both R_{vir} and V_c increase with mass, causing the dependence of j on halo mass to be stronger than for the disk radius, correctly approximating the trends in our simulations. For a more detailed quantitative model, one however has to account for the mass and redshift dependence of the halo concentration and the angular momentum distribution within haloes. Also, one has to postulate conservation of angular momentum of the gas during infall, an assumption we do not have to make in our detailed hydrodynamical simulations.

Owing to the increasing specific angular momentum as a function of halo and galaxy mass, one may wonder if a large part of the differences in Figure 13 is caused by the mass difference of galaxies inhabiting halos of the same mass. As we show in Section 3.3, in our highest resolution simulations the galaxy masses at a fixed halo mass are very similar between the two codes for $M_{\text{halo}} \lesssim 10^{11} M_{\odot}$. This means that trends with halo mass also directly reflect trends with galaxy mass. However, one needs to be more careful at higher masses where there is a systematic offset in

galaxy masses between AREPO and GADGET at a given halo mass. In Figure 14, we show the specific angular momentum for galactic baryons as a function of galaxy mass. In addition, we show a matched sample of galaxies in the mass range $10^{10} - 2 \times 10^{11} M_{\odot}$, connected with dashed lines to indicate corresponding differences in specific angular momentum for galaxies in the same collapsed structures. It is clear that the specific angular momentum of AREPO galaxies is systematically larger than for GADGET at a given galaxy mass. This trend is even clearer for our matched sample: for the large majority of galaxies, AREPO galaxies have much higher specific angular momentum than galaxies of the same mass in GADGET. In other words, the baryons that make galaxies in our moving mesh simulations either retain more angular momentum or are forming from baryons with systematically higher angular momentum.

Finally, we note that by looking at measurements of disk sizes as a function or resolution, we find that there appears to be a qualitative difference between our simulation techniques with respect to the sensitivity of predicted disk sizes on numerical resolution. In both codes, the sizes of the galactic gas distributions spuriously increase with poorer resolution, but this effect is somewhat stronger in AREPO. This basic trend is to be expected as poor spatial resolution will tend to lower the central densities in galaxies and make them puffy. In SPH, part of this trend is likely offset by the angular momentum transport caused by the artificial viscosity in SPH, which will tend to make galaxies more compact, as we discussed in Section 3.4.

To summarize, gaseous disks of AREPO galaxies are systematically larger than their counterparts in GADGET. AREPO galaxies show a higher degree of rotational support as measured by their specific angular momentum, indicating that they are more diskier and less dispersion-dominated. These differences are particularly prominent for the range of halo masses in which large disk galaxies are expected to form in the real Universe. We note that previous attempts to model disk galaxy formation in cosmological simulations with SPH often led to a too low specific angular momentum of simulated galaxies (e.g. Navarro & Steinmetz 2000). Higher resolution simulations of individual galaxies with SPH hinted that the problem might be less severe when the resolution is better (e.g. Governato et al. 2004, 2007). However, this has not been demonstrated yet for a large population of galaxies. Furthermore, we show that our moving-mesh simulations provide a dramatic improvement over corresponding SPH results and have much higher specific angular momentum at a given galaxy mass, facilitating formation of late-type galaxies.

4 DISCUSSION AND CONCLUSIONS

In this study, we have systematically compared results obtained for cosmological simulations of galaxy formation with the SPH code GADGET against the new moving-mesh code AREPO. The simulations started from identical initial conditions, employed the same high-resolution gravity solver, and used a completely equivalent modeling of the physics of radiative cooling, star formation and associated feedback processes, the latter being incorporated into a subresolution model for the multi-phase structure of the ISM. Hence the outcome of our simulations yields a direct test of the impact of hydrodynamical solvers on the predictions of cosmological galaxy formation simulations.

In Paper I of this series, we have focused on a comparison of the global baryonic properties predicted by the two simulation

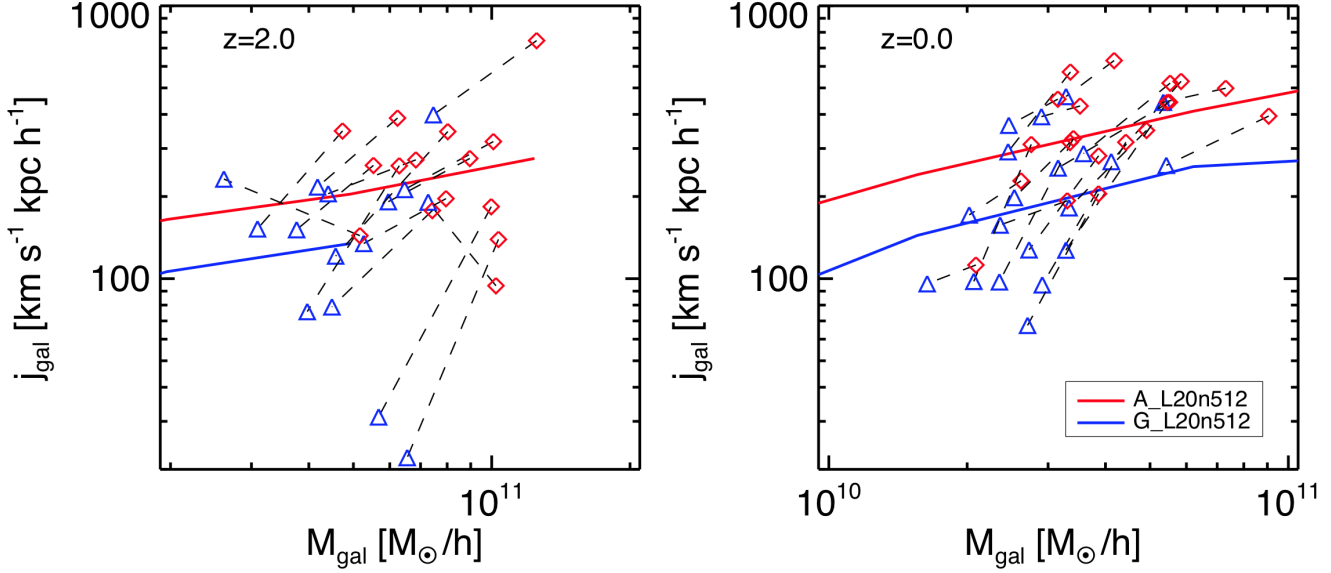


Figure 14. Specific angular momentum of galaxies (stars+gas) at $z = 2$ and $z = 0$, as a function of the galaxy mass. The measurement demonstrates that in AREPO (red lines) galaxies at a given mass have higher specific angular momentum than in GADGET (blue lines). Thick lines show the medians in 0.4 dex mass bins at $z = 2$, and 0.6 dex mass bin at $z = 0$. Symbols connected with thin dashed lines show a matched sample of galaxies in AREPO (red, diamonds) and GADGET (blue, triangles). The matched sample includes the first 20 galaxies from Figures 2 and 4 in Paper I, excluding galaxies undergoing major mergers, where the angular momentum changes rapidly. It is clear that for most of the galaxies in our simulations differences in specific angular momenta of galaxies are well above the trends expected from their mass differences.

techniques, while here we consider properties of individual galaxies. Reassuringly, we find that many of their properties are in fact in broad agreement, for example the galaxy mass functions are quite similar at low masses. However, when scrutinized in detail, and especially towards later times and in high mass systems, we find rather significant systematic differences in the predicted galaxy properties.

Specifically, massive haloes in AREPO host galaxies that are larger, diskier, more massive, and have a higher star formation rate than their GADGET counterparts. In the extreme end of the galaxy mass function, AREPO can accumulate up to a factor of ~ 2 more mass in central galaxies than GADGET. The moving-mesh galaxies also have a higher specific angular momentum, and the morphology of the gas surrounding the galaxies is clearly different, being much less clumpy than in the SPH code. These clumpy condensations of gas are largely absent in AREPO; instead, comparatively smooth gas disks are formed which tend to align better with the stellar disks.

There appears to be primarily a single driver for the higher star formation rates, lower central entropies and higher gas fractions in massive galaxies in AREPO. Multiple lines of evidence show (see also Paper I) that the hot gaseous haloes formed in AREPO cool out gas more efficiently than their counterparts in GADGET, causing in turn much higher star formation rates in the central galaxies of these haloes. We find that these different effective cooling rates occur despite the fact that the two codes create rather similar gas profiles in large haloes at low redshift, which do not suggest an a priori cause for a substantially different total cooling emission. In fact, we find that the culprit does not lie in a different cooling per se. It lies in a different *heating*. As we have shown in Paper I, the local dissipation rates in haloes simulated with SPH and the moving-mesh code are quite different. Whereas more entropy (and hence dissipative heating) is produced in the infall regions of haloes in

AREPO compared with GADGET, the opposite is true for most of the halo volume inside the virial region, and in particular in the outer parts of haloes where the cooling radius for many of these haloes lies. This dissipative heating offsets part of the cooling losses in SPH, reducing the strength of the cooling flows.

There are good reasons to believe that this heating effect in SPH is in fact spurious. First of all, as we demonstrate explicitly in Paper III, the standard formulation of SPH that we use here tends to suppress gas stripping out of infalling satellites, as well as any entropy mixing with background material. As a result, dense gaseous clumps penetrate further into haloes in GADGET upon infall, heating them through ram-pressure interactions at smaller radii than corresponding AREPO simulations, where material is stripped and mixed already at much larger radii. The stripping processes themselves, as well as the curved accretion shocks around haloes, inject subsonic and mildly transonic turbulence into the outer parts of haloes. However, as Bauer & Springel (2012) show, subsonic turbulent cascades are not represented in a physical way in SPH at the achievable resolution (unlike in the moving-mesh code). Instead, the turbulence is damped efficiently close to the injection scale.

In addition, there is significant viscous damping of small-scale subsonic noise in SPH. The latter is ultimately sourced by errors in SPH's gradient estimate (Abel 2011), which trigger jittering motions of the gas particles on the scale of the SPH kernel (Springel 2010b). If the artificial viscosity is increased, the amplitude of this sonic noise can be lowered, but the total dissipation through this effect stays nearly invariant (Bauer & Springel 2012). The dynamic environment around forming haloes can efficiently regenerate the SPH noise, such that its constant damping by the artificial viscosity constitutes a spurious heating source. Especially in the slow cooling regime encountered for large haloes at low redshift, this can then affect the cooling flows in haloes. We note that this problem is

neither easily cured by higher resolution, lower artificial viscosity, nor a larger number of SPH neighbors. What might help is a formulation of SPH that features a more accurate gradient estimate, which seems a prerequisite to eliminate the sub-sonic velocity noise.

The differences in cooling induce substantial differences in the SFRs of galaxies, which are largest for halo masses around $M_{\text{halo}} \sim 10^{12} h^{-1} M_{\odot}$ at $z = 0$, i.e. approximately at the mass scale of our own Milky Way galaxy. At this mass scale, we also find substantial differences of the predicted angular momentum content of both gas and stars, which is reflected in more extended disks galaxies forming in our moving-mesh simulations when compared to SPH. The differences in the gaseous disk sizes are apparent at all halo masses, but around $10^{12} h^{-1} M_{\odot}$ they are particularly large and reach a factor of ~ 3 . Because the angular momentum content of halo gas increases with time (see section 3.7), a more efficient gas supply at late times will lead to a relative increase of the specific angular momenta and sizes of galaxies. This suggests that the efficient late time cooling is not only increasing galaxy masses but is also a significant contributor to the differences in galaxy sizes, especially at mass ranges where the cooling differences are large. However, our results in Figure 14 show that this is not the only cause.

Also, we note that even low-mass galaxies have more extended gas distributions and higher gas content in the moving-mesh simulations when compared to SPH. These properties together with more efficient ram pressure stripping in moving-mesh runs (as we show in Paper III), will lead to a much larger mass loss from low-mass galaxies as they infall into more massive halos. This means that the fraction of the infalling material that will loose angular momentum via dynamical friction to dark matter halo will be much smaller in AREPO leading to a relative increase of specific angular momentum of galactic baryons with respect to GADGET.

The results we have presented in this paper hence clearly show that it does matter for simulations of galaxy formation which hydrodynamical solver is used. We find significant systematic offsets in the predicted properties of galaxies formed in GADGET and AREPO at all mass scales, but the most striking differences occur in haloes around $\sim 10^{12} h^{-1} M_{\odot}$. Here the more accurate hydrodynamics provided by AREPO leads to late-type galaxies that are large, disky, gas-rich, and have high star formation rates. Such galaxies, especially at late times, simply appear not to form in cosmological SPH simulations when the same physics is included. Our findings also suggest that AREPO is able to significantly alleviate the low angular momentum problem of galaxies formed in cosmological hydrodynamic simulations, which has been a long-standing issue in galaxy formation for the past two decades (e.g. Katz 1992; Navarro & Steinmetz 1997, 2000). Strong feedback mechanisms, however, appear to be needed to both regulate galaxy masses (e.g. Kereš et al. 2009b) and remove the low angular momentum baryons that form excessive bulges (e.g. van den Bosch 2001). Given the extended gaseous disks of galaxies in AREPO and diskier stellar morphology when compared to SPH results, it is likely that the strength and type of the required feedback discussed in previous SPH work needs to be revisited. This emphasizes that an accurate numerical treatment of hydrodynamics is a key factor for successful cosmological simulations that aim to form realistic galaxies in a complex environment.

ACKNOWLEDGMENTS

We would like to thank the referee, Fabio Governato, for constructive comments. The simulations in this paper were run on the Odyssey cluster supported by the FAS Science Division Research Computing Group at Harvard University. DK acknowledges support from NASA through Hubble Fellowship grant HSTHF-51276.01-A and NASA ATP NNX11AI97G. DS acknowledges NASA Hubble Fellowship through grant HST-HF-51282.01-A.

REFERENCES

- Abel T., 2011, MNRAS, 413, 271
- Agertz O., et al., 2007, MNRAS, 380, 963
- Bagla J. S., 2002, Journal of Astrophysics and Astronomy, 23, 185
- Barnes J., Efstathiou G., 1987, ApJ, 319, 575
- Barnes J., Hut P., 1986, Nature, 324, 446
- Bauer A., Springel V., 2012, MNRAS, 423, 2558
- Behroozi P. S., Conroy C., Wechsler R. H., 2010, ApJ, 717, 379
- Borgani S., Kravtsov A., 2009, ArXiv e-prints, 0906.4370
- Borgani S., Murante G., Springel V., Diaferio A., Dolag K., Moscardini L., Tormen G., Tornatore L., Tozzi P., 2004, MNRAS, 348, 1078
- Boylan-Kolchin M., Springel V., White S. D. M., Jenkins A., Lemson G., 2009, MNRAS, 398, 1150
- Brook C. B., Governato F., Roškar R., Stinson G., Brooks A. M., Wadsley J., Quinn T., Gibson B. K., Snaith O., Pilkington K., House E., Pontzen A., 2011, MNRAS, 415, 1051
- Bryan G. L., Norman M. L., Stone J. M., Cen R., Ostriker J. P., 1995, Computer Physics Communications, 89, 149
- Crain R. A., Eke V. R., Frenk C. S., Jenkins A., McCarthy I. G., Navarro J. F., Pearce F. R., 2007, MNRAS, 377, 41
- Crain R. A., Theuns T., Dalla Vecchia C., Eke V. R., Frenk C. S., Jenkins A., Kay S. T., Peacock J. A., Pearce F. R., Schaye J., Springel V., Thomas P. A., White S. D. M., Wiersma R. P. C., 2009, MNRAS, 399, 1773
- Creasey P., Theuns T., Bower R. G., Lacey C. G., 2011, MNRAS, p. 1030
- Croft R. A. C., Weinberg D. H., Katz N., Hernquist L., 1998, ApJ, 495, 44
- Daddi E., Dickinson M., Morrison G., Chary R., Cimatti A., Elbaz D., Frayer D., Renzini A., Pope A., Alexander D. M., Bauer F. E., Giavalisco M., Huynh M., Kurk J., Mignoli M., 2007, ApJ, 670, 156
- Davé R., 2008, MNRAS, 385, 147
- Davis M., Efstathiou G., Frenk C. S., White S. D. M., 1985, ApJ, 292, 371
- Dekel A., Birnboim Y., Engel G., Freundlich J., Goerdt T., Muncuoglu M., Neistein E., Pichon C., Teyssier R., Zinger E., 2009, Nature, 457, 451
- Diemand J., Kuhlen M., Madau P., Zemp M., Moore B., Potter D., Stadel J., 2008, Nature, 454, 735
- Dolag K., Borgani S., Murante G., Springel V., 2009, MNRAS, 399, 497
- D’Onghia E., Vogelsberger M., Faucher-Giguere C.-A., Hernquist L., 2010, ApJ, 725, 353
- Dutton A. A., van den Bosch F. C., Dekel A., 2010, MNRAS, 405, 1690
- Efstathiou G., 1992, MNRAS, 256, 43P
- Eisenstein D. J., Hu W., 1999, ApJ, 511, 5
- Ettori S., Dolag K., Borgani S., Murante t., 2006, MNRAS, 365, 1021

- Fall S. M., Efstathiou G., 1980, *MNRAS*, 193, 189
- Faucher-Giguère C.-A., Kereš D., Ma C.-P., 2011, *MNRAS*, 417, 2982
- Faucher-Giguère C.-A., Lidz A., Zaldarriaga M., Hernquist L., 2009, *ApJ*, 703, 1416
- Förster Schreiber N. M., et al., 2009, *ApJ*, 706, 1364
- Frenk C. S., et al., 1999, *ApJ*, 525, 554
- Gnedin N. Y., 2000, *ApJ*, 542, 535
- Governato F., Brook C., Mayer L., Brooks A., Rhee G., Wadsley J., Jonsson P., Willman B., Stinson G., Quinn T., Madau P., 2010, *Nature*, 463, 203
- Governato F., Mayer L., Wadsley J., Gardner J. P., Willman B., Hayashi E., Quinn T., Stadel J., Lake G., 2004, *ApJ*, 607, 688
- Governato F., Willman B., Mayer L., Brooks A., Stinson G., Valenzuela O., Wadsley J., Quinn T., 2007, *MNRAS*, 374, 1479
- Greif T. H., Springel V., White S. D. M., Glover S. C. O., Clark P. C., Smith R. J., Klessen R. S., Bromm V., 2011, *ApJ*, 737, 75
- Guedes J., Callegari S., Madau P., Mayer L., 2011, *ApJ*, 742, 76
- Guo Q., White S., Li C., Boylan-Kolchin M., 2010, *MNRAS*, 404, 1111
- Guo Q., White S. D. M., 2008, *MNRAS*, 384, 2
- Heitmann K., Lukić Z., Fasel P., Habib S., Warren M. S., White M., Ahrens J., Ankeny L., Armstrong R., O'Shea B., Ricker P. M., Springel V., Stadel J., Trac H., 2008, *Computational Science and Discovery*, 1, 015003
- Hernquist L., 1987, *ApJS*, 64, 715
- Hernquist L., Katz N., 1989, *ApJS*, 70, 419
- Hernquist L., Katz N., Weinberg D. H., Miralda-Escudé J., 1996, *ApJL*, 457, L51
- Hernquist L., Springel V., 2003, *MNRAS*, 341, 1253
- Heß S., Springel V., 2010, *MNRAS*, 406, 2289
- Hockney R. W., Eastwood J. W., 1981, *Computer Simulation Using Particles*. Computer Simulation Using Particles, New York: McGraw-Hill, 1981
- Hoeft M., Yepes G., Gottlöber S., Springel V., 2006, *MNRAS*, 371, 401
- Hutchings R. M., Thomas P. A., 2000, *MNRAS*, 319, 721
- Katz N., 1992, *ApJ*, 391, 502
- Katz N., Hernquist L., Weinberg D. H., 1992, *ApJL*, 399, L109
- Katz N., Weinberg D. H., Hernquist L., 1996, *ApJS*, 105, 19
- Kaufmann T., Bullock J. S., Maller A. H., Fang T., Wadsley J., 2009, *MNRAS*, 396, 191
- Kennicutt Jr. R. C., 1998, *ApJ*, 498, 541
- Keres D., 2007, PhD thesis, University of Massachusetts Amherst
- Kereš D., Katz N., Davé R., Fardal M., Weinberg D. H., 2009b, *MNRAS*, 396, 2332
- Kereš D., Katz N., Fardal M., Davé R., Weinberg D. H., 2009a, *MNRAS*, 395, 160
- Kereš D., Katz N., Weinberg D. H., Davé R., 2005, *MNRAS*, 363, 2
- Klypin A., Trujillo-Gomez S., Primack J., 2010, *ArXiv e-prints*, 1002.3660
- Komatsu E., et al., 2011, *ApJS*, 192, 18
- Kravtsov A. V., Klypin A., Hoffman Y., 2002, *ApJ*, 571, 563
- Kravtsov A. V., Nagai D., Vikhlinin A. A., 2005, *ApJ*, 625, 588
- Maller A. H., Dekel A., 2002, *MNRAS*, 335, 487
- Miralda-Escudé J., Cen R., Ostriker J. P., Rauch M., 1996, *ApJ*, 471, 582
- Mitchell N. L., McCarthy I. G., Bower R. G., Theuns T., Crain R. A., 2009, *MNRAS*, 395, 180
- Mo H. J., Mao S., White S. D. M., 1998, *MNRAS*, 295, 319
- Müller E., Steinmetz M., 1995, *Computer Physics Communications*, 89, 45
- Murali C., Katz N., Hernquist L., Weinberg D. H., Davé R., 2002, *ApJ*, 571, 1
- Navarro J. F., Ludlow A., Springel V., Wang J., Vogelsberger M., White S. D. M., Jenkins A., Frenk C. S., Helmi A., 2010, *MNRAS*, 402, 21
- Navarro J. F., Steinmetz M., 1997, *ApJ*, 478, 13
- Navarro J. F., Steinmetz M., 2000, *ApJ*, 538, 477
- Noeske K. G., et al., 2007, *ApJL*, 660, L43
- Ocvirk P., Pichon C., Teyssier R., 2008, *MNRAS*, 390, 1326
- Okamoto T., Gao L., Theuns T., 2008, *MNRAS*, 390, 920
- Okamoto T., Jenkins A., Eke V. R., Quilis V., Frenk C. S., 2003, *MNRAS*, 345, 429
- O'Shea B. W., Nagamine K., Springel V., Hernquist L., Norman M. L., 2005, *ApJS*, 160, 1
- Pakmor R., Bauer A., Springel V., 2011, *MNRAS* accepted, arXiv:1108.1792
- Pearce F. R., Jenkins A., Frenk C. S., Colberg J. M., White S. D. M., Thomas P. A., Couchman H. M. P., Peacock J. A., Efstathiou G., The Virgo Consortium 1999, *ApJL*, 521, L99
- Peebles P. J. E., 1969, *ApJ*, 155, 393
- Petkova M., Springel V., 2011, *MNRAS*, 415, 3731
- Price D. J., 2008, *Journal of Computational Physics*, 227, 10040
- Puchwein E., Springel V., Sijacki D., Dolag K., 2010, *MNRAS*, 406, 936
- Rasio F. A., 2000, *Progress of Theoretical Physics Supplement*, 138, 609
- Read J. I., Hayfield T., 2012, *MNRAS*, 422, 3037
- Read J. I., Hayfield T., Agertz O., 2010, *MNRAS*, 405, 1513
- Regan J. A., Haehnelt M. G., Viel M., 2007, *MNRAS*, 374, 196
- Robertson B. E., Kravtsov A. V., Gnedin N. Y., Abel T., Rudd D. H., 2010, *MNRAS*, 401, 2463
- Ryu D., Ostriker J. P., Kang H., Cen R., 1993, *ApJ*, 414, 1
- Saitoh T. R., Makino J., 2012, *ApJ* submitted, arXiv:1202.4277
- Salim S., et al., 2007, *ApJS*, 173, 267
- Scannapieco C., Wadepuhl M., Parry O. H., Navarro J. F., Jenkins A., Springel V., Teyssier R., et al., 2012, *MNRAS*, 423, 1726
- Seljak U., Makarov A., McDonald P., et al., 2005, *Phys. Rev. D*, 71, 103515
- Sijacki D., Vogelsberger M., Kereš D., Springel V., Hernquist L., 2011, *MNRAS* in press, arXiv:1109.3468
- Somerville R. S., Barden M., Rix H.-W., Bell E. F., Beckwith S. V. W., Borch A., Caldwell J. A. R., Häußler B., Heymans C., Jahnke K., Jooe S., McIntosh D. H., Meisenheimer K., Peng C. Y., Sánchez S. F., Wisotzki L., Wolf C., 2008, *ApJ*, 672, 776
- Springel V., 2005, *MNRAS*, 364, 1105
- Springel V., 2010a, *MNRAS*, 401, 791
- Springel V., 2010b, *ARA&A*, 48, 391
- Springel V., Hernquist L., 2002, *MNRAS*, 333, 649
- Springel V., Hernquist L., 2003a, *MNRAS*, 339, 289
- Springel V., Hernquist L., 2003b, *MNRAS*, 339, 312
- Springel V., Wang J., Vogelsberger M., Ludlow A., Jenkins A., Helmi A., Navarro J. F., Frenk C. S., White S. D. M., 2008, *MNRAS*, 391, 1685
- Springel V., White S. D. M., Jenkins A., Frenk C. S., Yoshida N., Gao L., Navarro J., Thacker R., Croton D., Helly J., Peacock J. A., Cole S., Thomas P., Couchman H., Evrard A., Colberg J., Pearce F., 2005, *Nature*, 435, 629
- Springel V., White S. D. M., Tormen G., Kauffmann G., 2001, *MNRAS*, 328, 726

- Springel V., Yoshida N., White S. D. M., 2001, *New Astronomy*, 6, 79
- Tasker E. J., Brunino R., Mitchell N. L., Michielsen D., Hopton S., Pearce F. R., Bryan G. L., Theuns T., 2008, *MNRAS*, 390, 1267
- Teyssier R., 2002, *A&A*, 385, 337
- Thoul A. A., Weinberg D. H., 1996, *ApJ*, 465, 608
- Toomre A., Toomre J., 1972, *ApJ*, 178, 623
- Torrey P., Vogelsberger M., Sijacki D., Springel V., Hernquist L., 2011, *MNRAS* submitted, arXiv:1110.5635
- van den Bosch F. C., 2001, *MNRAS*, 327, 1334
- Vazza F., Dolag K., Ryu D., Brunetti G., Gheller C., Kang H., Pfrommer C., 2011, *MNRAS*, 418, 960
- Vogelsberger M., Sijacki D., Kereš D., Springel V., Hernquist L., 2011, *MNRAS* in press, arXiv:1109.1281
- Wadsley J. W., Stadel J., Quinn T., 2004, *New Astronomy*, 9, 137
- Wadsley J. W., Veeravalli G., Couchman H. M. P., 2008, *MNRAS*, 387, 427
- Weinberg D. H., Hernquist L., Katz N., 1997, *ApJ*, 477, 8
- White S. D. M., Frenk C. S., 1991, *ApJ*, 379, 52
- Wuyts S., Förster Schreiber N. M., Lutz D., Nordon R., Berta S., et al., 2011, *ApJ*, 738, 106